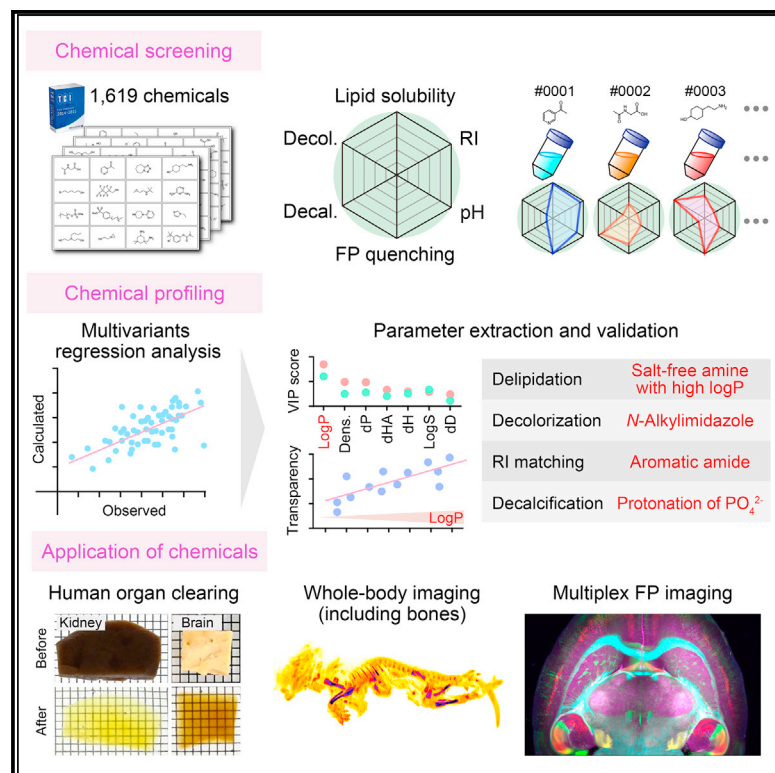


Cell Reports

Chemical Landscape for Tissue Clearing Based on Hydrophilic Reagents

Graphical Abstract



Authors

Kazuki Tainaka, Tatsuya C. Murakami, Etsuo A. Susaki, ..., Masashi Fukayama, Akiyoshi Kakita, Hiroki R. Ueda

Correspondence

uedah-tyk@umin.ac.jp

In Brief

Tainaka et al. describe a strategy for developing hydrophilic tissue-clearing reagents based on comprehensive chemical profiling. The strategic integration of optimal chemical cocktails provided a series of CUBIC protocols, which enable the 3D imaging of the mammalian body and large primate and human tissues.

Highlights

- Comprehensive chemical profiling of hydrophilic chemicals for tissue clearing
- Strategic integration of optimal chemical cocktails for rational clearing protocols
- Large-tissue clearing and cell-resolution imaging of tissues by CUBIC protocols
- Virtual multiplex imaging of fluorescent protein-expressing mouse brains



Chemical Landscape for Tissue Clearing Based on Hydrophilic Reagents

Kazuki Tainaka,^{1,2,3,20} Tatsuya C. Murakami,^{1,20} Etsuo A. Susaki,^{1,2,4} Chika Shimizu,² Rie Saito,⁵ Kei Takahashi,⁶ Akiko Hayashi-Takagi,^{4,7} Hiroshi Sekiya,⁸ Yasunobu Arima,⁹ Satoshi Nojima,¹⁰ Masako Ikemura,¹¹ Tetsuo Ushiku,¹¹ Yoshihiro Shimizu,¹² Masaaki Murakami,⁹ Kenji F. Tanaka,¹³ Masamitsu Iino,^{8,14} Haruo Kasai,^{15,19} Toshikuni Sasaoka,¹⁶ Kazuto Kobayashi,¹⁷ Kohei Miyazono,⁶ Eiichi Morii,¹⁰ Tadashi Isa,¹⁸ Masashi Fukayama,¹¹ Akiyoshi Kakita,⁵ and Hiroki R. Ueda^{1,2,19,21,*}

¹Department of Systems Pharmacology, Graduate School of Medicine, The University of Tokyo, 7-3-1 Hongo, Bunkyo-ku, Tokyo 113-0033, Japan

²Laboratory for Synthetic Biology, RIKEN Center for Biosystems Dynamics Research, 1-3 Yamadaoka, Suita, Osaka 565-5241, Japan

³Department of System Pathology for Neurological Disorders, Brain Research Institute, Niigata University, 1-757 Asahimachidori, Chuo-ku, Niigata 951-8585, Japan

⁴PRESTO, Japan Science and Technology Agency (JST), 4-1-8 Honcho, Kawaguchi, Saitama 332-0012, Japan

⁵Department of Pathology, Brain Research Institute, Niigata University, 1-757 Asahimachidori, Chuo-ku, Niigata 951-8585, Japan

⁶Department of Molecular Pathology, Graduate School of Medicine, The University of Tokyo, 7-3-1 Hongo, Bunkyo-ku, Tokyo 113-0033, Japan

⁷Laboratory of Medical Neuroscience, Institute for Molecular and Cellular Regulation, Gunma University, 3-39-15 Showacho, Maebashi, Gunma 371-8512, Japan

⁸Department of Pharmacology, Graduate School of Medicine, The University of Tokyo, 7-3-1 Hongo, Bunkyo-ku, Tokyo 113-0033, Japan

⁹Division of Psychoimmunology, Institute of Genetic Medicine, Graduate School of Medicine, Hokkaido University, Kita-15, Nishi-7, Kita-ku, Sapporo, Hokkaido 060-0815, Japan

¹⁰Department of Pathology, Osaka University Graduate School of Medicine, 2-2 Yamadaoka, Suita, Osaka 565-0871, Japan

¹¹Department of Pathology, Graduate School of Medicine, The University of Tokyo, 7-3-1 Hongo, Bunkyo-ku, Tokyo 113-0033, Japan

¹²Laboratory for Cell-Free Protein Synthesis, RIKEN Center for Biosystems Dynamics Research, 6-2-3, Furuedai, Suita, Osaka 565-0874, Japan

¹³Department of Neuropsychiatry, Keio University School of Medicine, 35 Shinanomachi, Shinjuku-ku, Tokyo 160-8582, Japan

¹⁴Division of Cellular and Molecular Pharmacology, Nihon University School of Medicine, 30-1 Oyaguchikami-cho, Itabashi-ku, Tokyo 173-8610, Japan

¹⁵Laboratory of Structural Physiology, Center for Disease Biology and Integrative Medicine, Graduate School of Medicine, The University of Tokyo, 7-3-1 Hongo, Bunkyo-ku, Tokyo 113-0033, Japan

¹⁶Department of Comparative and Experimental Medicine, Brain Research Institute, Niigata University, 1-757 Asahimachidori, Chuo-ku, Niigata 951-8585, Japan

¹⁷Department of Molecular Genetics, Institute of Biomedical Sciences, Fukushima Medical University School of Medicine, 1 Hikarigaoka, Fukushima, Fukushima 960-1295, Japan

¹⁸Department of Neuroscience, Graduate School of Medicine and Faculty of Medicine, Kyoto University, Yoshida-konoe-cho, Sakyo-ku, Kyoto 606-8501, Japan

¹⁹International Research Center for Neurointelligence (WPI-IRCN), UTIAS, The University of Tokyo, Tokyo, Japan

²⁰These authors contributed equally

²¹Lead Contact

*Correspondence: uedah-ky@umin.ac.jp
<https://doi.org/10.1016/j.celrep.2018.07.056>

SUMMARY

We describe a strategy for developing hydrophilic chemical cocktails for tissue delipidation, decoloring, refractive index (RI) matching, and decalcification, based on comprehensive chemical profiling. More than 1,600 chemicals were screened by a high-throughput evaluation system for each chemical process. The chemical profiling revealed important chemical factors: salt-free amine with high octanol/water partition-coefficient (logP) for delipidation, *N*-alkylimidazole for decoloring, aromatic amide for RI matching, and protonation of phosphate ion for decalcification. The strategic integration of optimal chemical cocktails provided a series of CUBIC

(clear, unobstructed brain/body imaging cocktails and computational analysis) protocols, which efficiently clear mouse organs, mouse body including bone, and even large primate and human tissues. The updated CUBIC protocols are scalable and reproducible, and they enable three-dimensional imaging of the mammalian body and large primate and human tissues. This strategy represents a future paradigm for the rational design of hydrophilic clearing cocktails that can be used for large tissues.

INTRODUCTION

To examine an entire mammalian body as functional assemblies of individual cells is an important goal in biology and medicine.



The systematic identification of cellular properties in their physiological context helps us understand the complex cellular networks in the body. To this end, three-dimensional (3D) imaging techniques that use tissue clearing and are compatible with various labeling techniques are promising approaches. The tissue-clearing step is critical for determining the quality of the subsequent acquired image and the feasibility of image processing. Since tissue-clearing methods were first reported more than a century ago (Spalteholz, 1914), the field has expanded dramatically (Susaki and Ueda, 2016; Tainaka et al., 2016). Several scalable tissue-clearing protocols with high clearing performance that can be used with 3D-imaging procedures were recently developed. The perfusion-assisted agent release *in situ*-passive clarity technique (PARS-PACT) protocol enables whole adult mouse body clearing (Trewick et al., 2015; Yang et al., 2014). The clear, unobstructed brain/body imaging cocktails and computational analysis (CUBIC) protocol enables whole organ and body imaging with single-cell resolution (Kubota et al., 2017; Susaki et al., 2015; Tainaka et al., 2014). The system-wide control of interaction time and kinetics of chemicals (SWITCH) protocol achieves large (>1 cm³) tissue clearing, including that of whole adult primate brain and large human tissue samples (Murray et al., 2015). The ultimate DISCO (uDISCO) protocol enables whole adult rat body imaging and the visualization of high-resolution images of bone marrow in the entire mouse body without chemical decalcification (Pan et al., 2016). These protocols and related technologies have greatly advanced the applicability of 3D imaging (Ando et al., 2014; Belle et al., 2014, 2017; Doerr et al., 2017; Liebmann et al., 2016; Renier et al., 2014, 2016). However, many clearing methods are still empirical protocols based on serendipitously discovered effective chemicals and *ad hoc* chemical combinations. In contrast, to achieve improved tissue-clearing techniques, it is important to understand the effective functional groups and chemical properties of each clearing step. Such comprehensive chemical profiling would lead to rationally designed clearing cocktails. Although organic solvents were systematically screened by Spalteholz and his successors (Becker et al., 2012; Pan et al., 2016), clearing cocktails based on hydrophilic chemicals are still under development.

In this study, we applied a strategy for designing hydrophilic chemical cocktails optimized for individual chemical parameters. To achieve the scalable clearing of large primate and human tissue samples and of mammalian bodies including bone tissue in aqueous media, we considered a series of chemical processes, including delipidation, decoloring, refractive index (RI) matching, and decalcification. Using high-throughput evaluation systems suitable for each chemical process, we comprehensively screened >1,600 hydrophilic chemicals. Chemical profiling of the screened chemicals revealed important chemical factors: salt-free amine with high logP for delipidation, *N*-alkylimidazole for decoloring, aromatic amide for RI matching, and protonation of phosphate ion for decalcification. Finally, by strategically integrating optimal chemical cocktails, we obtained a series of updated CUBIC protocols that efficiently cleared mouse organs, mouse body including bone, and large primate tissue samples, including marmoset brain and human tissue samples >10 cm³. The CUBIC-treated tissues were transparent

enough that almost all of the cells could be detected at the whole-organ scale. In addition, a fluorescent protein (FP)-compatible CUBIC protocol enabled the visualization of various fluorescent labels.

RESULTS

Rational Chemical Profiles for Tissue Clearing Obtained by Comprehensively Screening >1,600 CUBIC Chemicals

To comprehensively screen chemicals for hydrophilic chemical-based clearing methods, >1,600 commercially available chemical candidates were chosen based on their potential solubility in aqueous media (Figure 1A; Table S1). If a chemical was sufficiently soluble in water, then a 10% (w/w) stock solution was prepared in deionized water. These chemical solutions were then subjected to a series of easy and high-throughput CUBIC assays (for pH, fluorescent quenching of FPs, lipid solubility, decoloring, RI matching, and decalcification) (Figures 1B–1F; Table S2). After the first chemical screening, we narrowed down the candidates by a second evaluation using real tissue (Table S2). The pH of each stock solution was estimated by the colorimetric analysis of pH-indicator paper (Figures S1A–S1C). To evaluate the quenching effect of each chemical, recombinant EGFP and Sirius were used as described previously (Figures 1F, S1D, and S1E) (Susaki et al., 2014).

Delipidation and Decoloring

Qualitatively, the lipid solubility of a chemical is inversely correlated with the turbidity of a fixed brain suspension treated with the chemical (Susaki et al., 2014). Thus, we obtained lipid solubility scores from the optical density 600 (OD₆₀₀) of a mixture of brain suspension and each 10% (w/w) chemical solution (Figure 1B). We classified the chemicals into three groups: detergents, salts, and other non-detergent and salt-free chemicals. Anionic and non-ionic detergents with a suitable logP (octanol-water partition coefficient) value of the hydrophobic group exhibited significantly higher lipid solubility, while organic salts were less effective (Figures S2A–S2C). The other water-soluble chemicals were subjected to further functional chemical profiling. Aliphatic amines, amino alcohols, and amino ethers were found to be the most effective functional groups for lipid solubility (Figure 2A). A basic condition (pH >10) was significantly superior to an acidic one (pH < 6) (Figure 2B). To determine the effective chemical parameters for delipidation, we used a multivariate linear regression model. We prepared a series of parameters consisting of three classes, related to functional groups, solubility (calculated by Hansen's solubility parameters [Hansen, 2007]), and structure and topology (Figure S1F). Figure S1G shows examples of how we counted the functional groups. Our model revealed logP to be the most influential property (Figure 2C). In actuality, the lipid solubility score of less polar amines (logP ≥ -2.0) was linearly correlated with their logP (Figure 2D). Therefore, water-soluble, relatively hydrophobic, and uncharged amine derivatives had the potential for high lipid solubility. Next, we measured the residual phospholipid and cholesterol contents of mouse brains treated with the

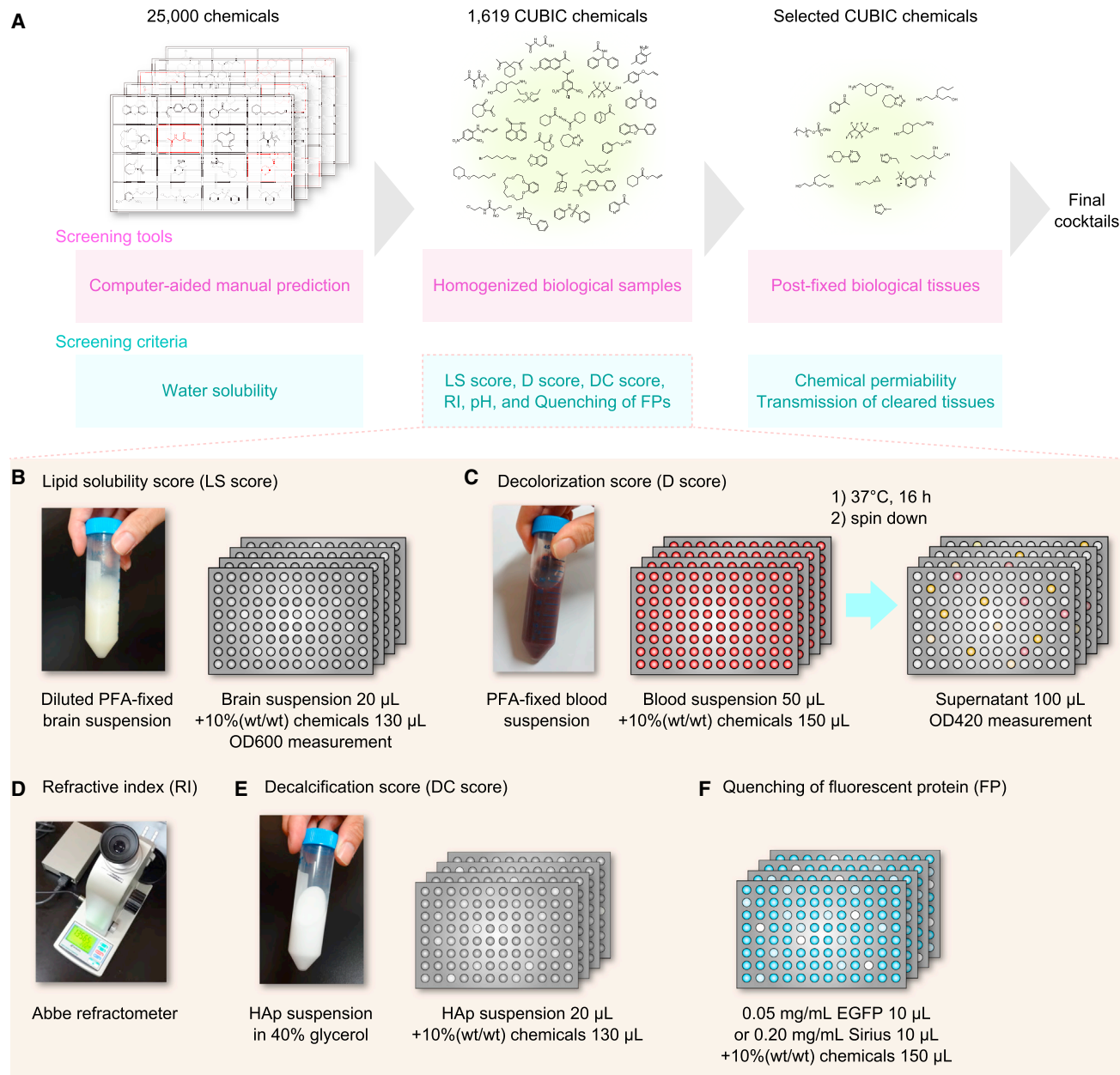


Figure 1. Strategy for Screening >1,600 CUBIC Chemicals

(A) Experimental overview of the screening of >1,600 CUBIC chemicals. In the first *in vitro* screening, six chemical properties of potentially water-soluble CUBIC chemicals were quantitatively evaluated. In the second evaluation, using real tissue samples, the candidate chemicals were narrowed down.

(B–F) Experimental scheme for the high-throughput chemical screening of delipidation (B), decoloring (C), RI measurement (D), decalcification (E), and FP fluorescence measurement (F). A popular FP, EGFP, and a pH-insensitive FP, Sirius, were used. PFA, paraformaldehyde.

See also [Figures S1](#) and [S8](#) and [Table S1](#).

chemicals and evaluated the relative transmittance of these brains after RI matching with the modified *ScaleCUBIC-2* ([Figures 2E](#) and [S2D](#)). The delipidation efficiency, especially for the phospholipid content, was correlated with the final tissue transparency, indicating that delipidation is essential for thorough tissue clearing. Aliphatic amines exhibited a much better delipidation efficiency than did amino alcohols

or detergents ([Figure 2F](#)). More important, the logP value of these chemicals could predict the final transparency of the chemically treated brain ([Figure S2E](#)). Therefore, the variability within aliphatic amines and *N*-alcohols could be explained by their logP value. It is likely that detergents were inferior to aliphatic amines in tissue permeability despite their high potential lipophilicity.

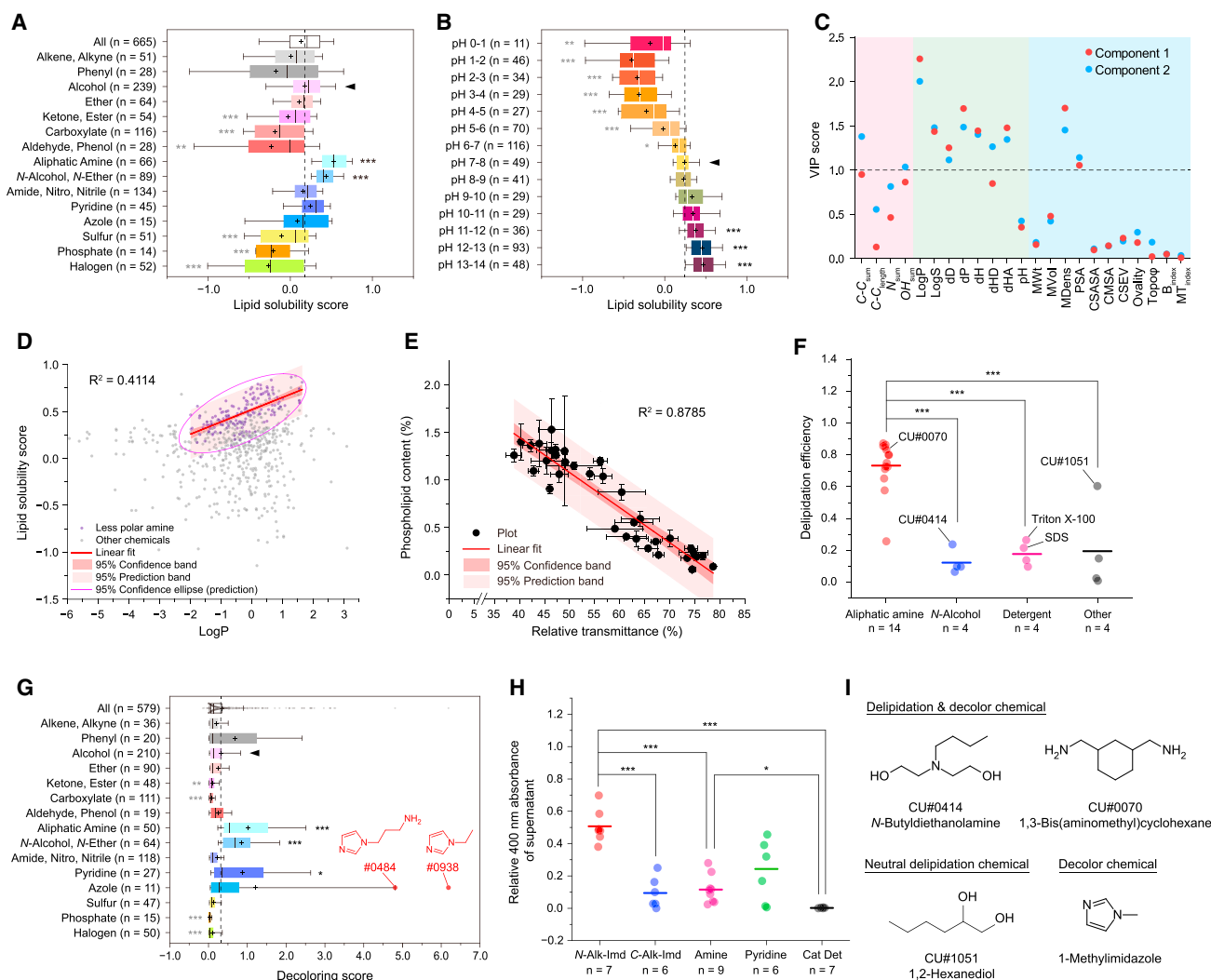


Figure 2. Comprehensive CUBIC Chemical Profiling for Delipidation and Decoloring

(A and B) Dependency of the lipid solubility score on the chemical functional group (A) and pH (B), compared with the alcohol group and pH 7–8, respectively. (C) The variable importance projection (VIP) scores of two major partial least-squares (PLS) components for each variance. (D) Scatterplot of the logP and lipid solubility score for water-soluble CUBIC chemicals. The logP of less polar amines (including aliphatic amines, *N*-alcohols, and *N*-ethers with logP ≥ -2.0) was correlated with their lipid solubility score. (E) Scatterplot of the relative transmittance and phospholipid content of brain hemispheres of adult mice treated with highly lipid-soluble chemicals. Data are means \pm SDs (n = 2). (F) Delipidation efficiency of the aliphatic amines, amino alcohol (*N*-alcohol), detergents, and others in (E). (G) Dependency of the decoloring score on chemical functional groups compared with the alcohol group. (H) Decoloring efficiency for adult mouse spleen of *N*-alkylimidazole (*N*-Alk-Imd), *C*-alkylimidazole (*C*-Alk-Imd), amine, pyridine, and cationic detergent (Cat Det). (I) Representative chemical candidates for delipidation and/or decoloring. Box and whisker plots showing the 25th–75th percentile (boxes), 10th–90th percentile (whiskers), median (vertical lines), and mean (cross). * $p < 0.05$, ** $p < 0.01$, and *** $p < 0.001$. See also Figures S1 and S2, Table S2, and the STAR Methods.

We established a high-throughput screening system for the decoloring ability of chemicals by measuring the OD₄₂₀ of the supernatant obtained from a fixed blood suspension treated with the chemical (Tainaka et al., 2014) (Figure 1C). Cationic detergents tended to elute heme more efficiently, while organic salts were significantly less active (Figures S2F and S2G). The pH dependency of the decoloring was also similar to that of the lipid solubility (Figure S2H). The functional chemical profiling of the

other water-soluble chemicals revealed chemical groups similar to those identified in the lipid solubility assay (Figure 2G). We noted that *N*-alkylimidazoles (1-ethylimidazole [CU#0938] and 1-(3-aminopropyl)imidazole [CU#0484]) were the most effective decoloring chemicals. Next, we investigated how well these chemicals decolorized heme-rich mouse spleen by soaking this tissue in the chemical solution and measuring the OD₄₀₀ of the supernatant. *N*-Alkylimidazole was found to be the best

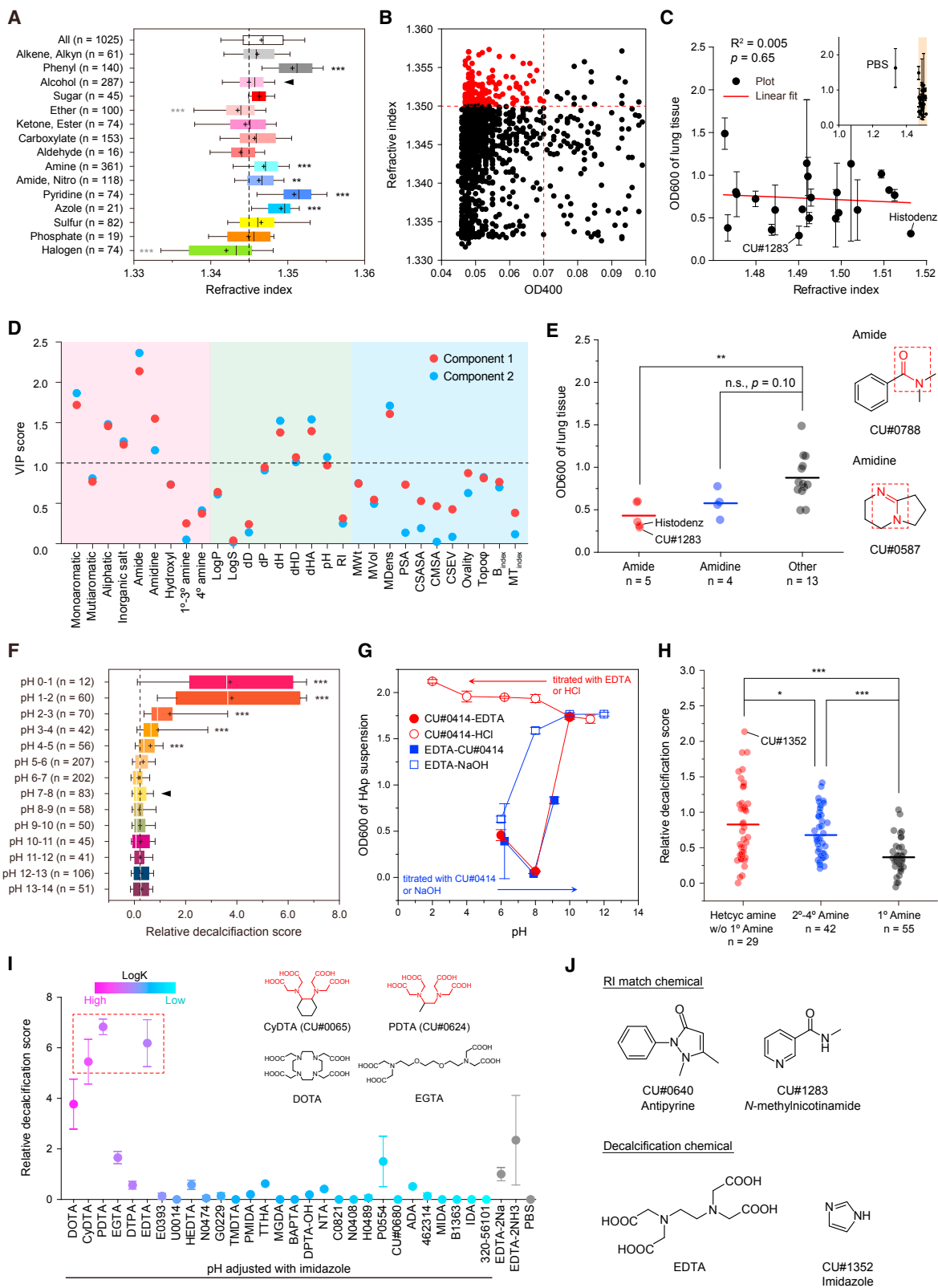


Figure 3. Comprehensive CUBIC Chemical Profiling of RI Matching and Decalcification

(A) Dependency of RI on functional groups compared with the alcohol group.

(B) Scatterplot of 400-nm absorbance and RI. Less colored ($OD_{400} < 0.07$) and high RI ($RI > 1.350$) CUBIC chemicals were chosen for further screening.

(legend continued on next page)

decoloring chemical among several chemical categories (Figure 2H). However, since *N*-alkylimidazole showed a low delipidation efficiency, we further analyzed decoloring chemicals that had a high delipidation efficiency. We applied the multivariate linear regression model to amine groups, and the model revealed the chain length to be the most influential parameter (Figure S2I). Multiple polar groups (e.g., $-\text{NH}_2$ and $-\text{OH}$) and a longer chain length between the polar groups ($C-C_{\text{length}} \geq 3$) were associated with efficient decoloring ability (Figure S2J).

Among the screened chemicals, we highlight the following four chemicals: *N*-butyldiethanolamine and 1,3-bis(aminomethyl)cyclohexane are a cost-effective, high-performance amino alcohol and an aliphatic amine, respectively; 1,2-hexanediol is an exceptional aliphatic diol that acts as a neutral delipidation chemical; and 1-methylimidazole is especially effective for tissue decoloring (Figure 2I).

RI Matching

To clarify whether the RI value of the medium itself is important for the final transparency or whether specific chemical groups are important for RI homogenization, we used a non-biased approach to determine the best RI-matched chemicals. To develop an alternative high-RI medium based on hydrophilic chemicals, we selected candidate chemicals that had high water solubility and a high RI value per unit weight, because the RI value of aqueous medium increases according to the solute concentration. Chemical profiling of the RI values of 10% (w/w) chemical solutions with an Abbe refractometer (Figure 1D) revealed that aromatic groups (phenyl, pyridine, and azole groups) exhibited higher RI values among the chemical groups (Figure 3A). We then chose candidate chemicals with high RI values (≥ 1.350) and low absorbance ($\text{OD}_{400} < 0.07$) to avoid incoming light absorption by the medium itself (Figure 3B). We chose 21 extremely water-soluble RI-matching candidates, including Histodenz (soluble in water at 60–70 wt%; Sigma-Aldrich), whose RIs ranged from 1.47 to 1.52. To examine the clearing performance of these chemicals qualitatively, the OD_{600} of small pieces of chemically treated mouse lung was measured (Figure 3C). The RI values of the mounting medium showed no correlation with the tissue transparency, suggesting that the clearing performance does not depend solely on the RI value of the medium but does reflect some chemical properties of the constituent. We further applied the multivariate linear regres-

sion model to this result. The amide group showed a significantly higher clearing performance than the other chemical groups (Figures 3D, 3E, and S2K). Finally, we introduced antipyrine and CU#1283 (*N*-methylnicotinamide) as RI-matching chemicals (Figure 3J, top). *N*-Methylnicotinamide had the highest clearing performance among the candidates. In addition to its high clearing performance, antipyrine avoided tissue shrinkage, even with a dense solution, because this chemical causes tissue swelling (Murakami et al., 2018).

Decalcification

Inorganic bone mineral mostly consists of carbonated hydroxyapatite (HAp). Thus, we developed an HAp-based screening system to identify potent decalcification chemicals by measuring the OD_{600} of a chemically treated HAp suspension (Figure 1E). The OD_{600} of HAp suspensions was linearly correlated with the HAp concentration below 10 mg/mL (Figure S2L). Decalcification was strongly promoted by an acidic condition, especially below pH 2.0 (Figure 3F). Because phosphate ion has a $\text{p}K_{\text{a}1}$ value of 2.12 (Weast, 1983), the facilitated decalcification under acidic conditions may have been associated with an equilibrium shift in the phosphate ion. Since acid-based decalcification was incompatible with many of the other tissue-clearing steps, we sought other decalcifying chemicals that would act in neutral medium. We found that the decalcification efficiency of a 10 wt% EDTA-Na solution markedly decreased over pH 8.0 (Figure 3G). Although this result apparently contradicts the pH dependency of the stability constant of EDTA for the calcium ion (Harris, 2011), an unexpected pH dependency was already reported for both decalcification and demineralization by EDTA (Kiviranta et al., 1980; Serper and Calt, 2002). This may also reflect the equilibrium shift of the phosphate ion because of its $\text{p}K_{\text{a}2}$ value of 7.21. It is also noteworthy that a 10 wt% EDTA solution neutralized with *N*-butyldiethanolamine exhibited significantly higher decalcification efficiency at pH 8.0 than did EDTA-Na (Figure 3G), implying that decalcification would be greatly facilitated by neutralization with an organic base instead of an inorganic base (NaOH). Therefore, we screened EDTA-related acids and *N*-butyldiethanolamine-related organic bases among the listed chemicals. While EDTA-related calcium chelators including CU#0065 (*trans*-1,2-diaminocyclohexane-*N,N,N',N'*-tetraacetic acid monohydrate [CyDTA]) and CU#0624 (1,2-diaminopropane-*N,N,N',N'*-tetraacetic acid [PDTA]) were the most effective

(C) Scatterplot of the RI value of concentrated solutions of 22 candidate chemicals and the OD_{600} of small pieces of mouse lung treated with those chemicals. Data are means \pm SDs ($n = 2$).

(D) VIP scores of two major components for each variance.

(E) The 22 chemicals in (C) were divided into three groups: amides, amidines, and others, and the OD_{600} of lungs treated with these groups were compared. Amide and amidine groups are shown in red dashed-line boxes at right.

(F) Dependency of relative decalcification score on pH compared with pH 7–8.

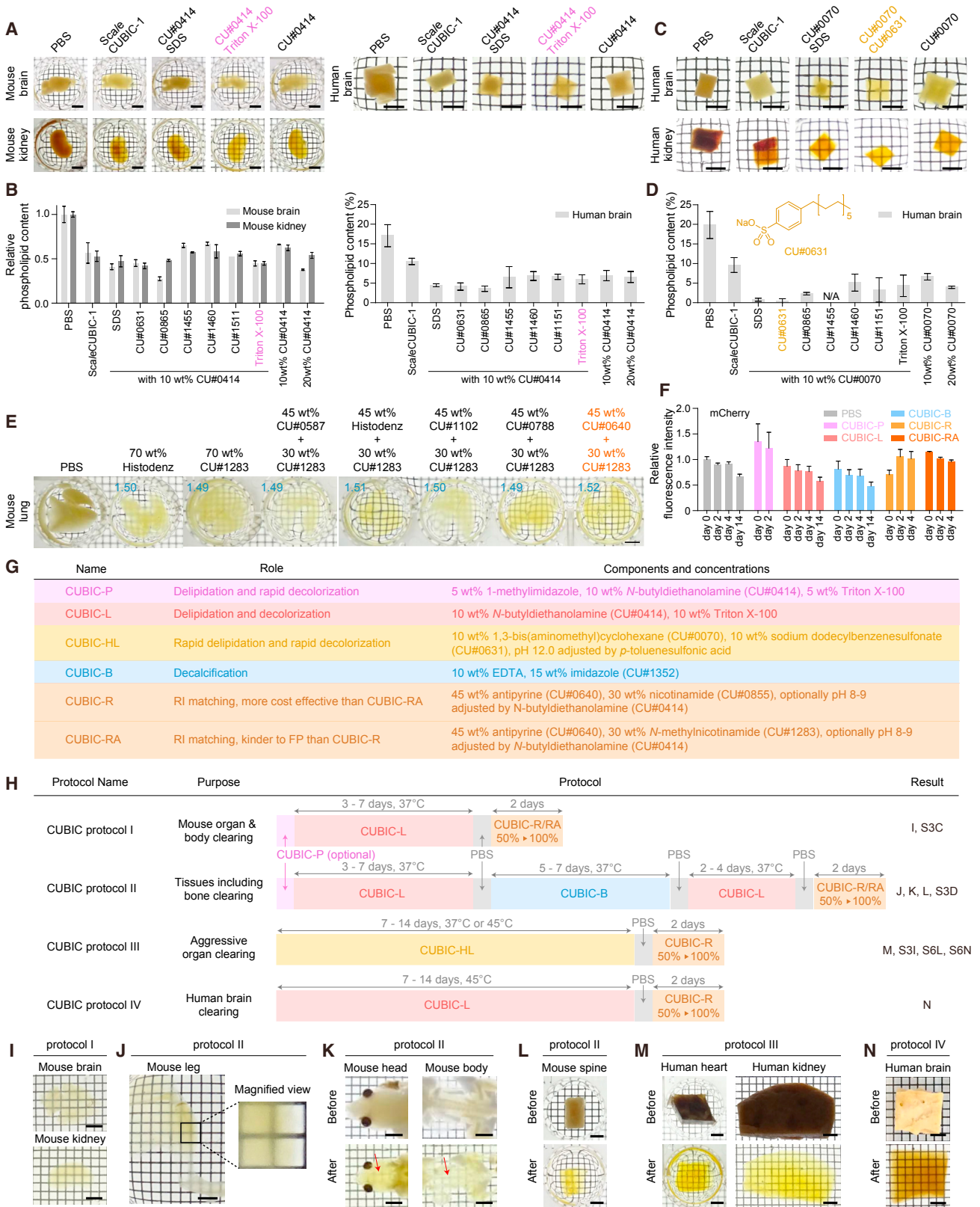
(G) pH dependence of OD_{600} of chemically treated HAp suspension. Data are means \pm SDs ($n = 3$). *N*-butyldiethanolamine (CU#0414) 10 wt% titrated with EDTA or HCl and EDTA 10 wt% titrated with CU#0414 or NaOH were used.

(H) Relative decalcification scores of EDTA-based cocktails (pH 7–8) neutralized with various counter-bases including heterocyclic amines without primary amine (Hetcyc amine w/o 1° amine), secondary and tertiary amines and quaternary ammoniums (2°–4° amine), and other amines including primary amine (1° amine).

(I) Relative decalcification score of EDTA derivatives. Data are means \pm SDs ($n = 3$). Chemicals are presented in descending order of $\log K$. Chemical ID is a typical abbreviation or vendor catalog number. The top three chemicals shared a common EDTA structure (red).

(J) Chemical candidates for high RI matching medium and decalcification cocktails consisting of EDTA and imidazole (CU#1352). Box and whisker plots show 25th–75th percentiles (boxes), 10th–90th percentiles (whiskers), median (horizontal lines), and mean (cross). * $p < 0.05$, ** $p < 0.01$, and *** $p < 0.001$.

See also Figures S1 and S2, Table S2, and the STAR Methods.



(legend on next page)

decalcification acids, heterocyclic amines without a primary amine were found to be the optimal organic base (Figures S2M and 3H). EDTA-related chemicals (e.g., EDTA, CyDTA, and PDTA) were still superior to other chelators, even to 1,4,7,10-tetraazacyclododecane-1,4,7,10-tetraacetic acid (DOTA) and EGTA, which have higher stability constants for calcium ion (logK) than EDTA (Figure 3I), suggesting that the specific chemical nature of EDTA may play an important role in an organic base-assisted decalcification. Collectively, the combined cocktail of EDTA and imidazole appeared to be the optimal decalcification solution (Figure 3J, bottom).

Rapid and Scalable Tissue Clearing by Updated CUBIC Protocols Combining Various CUBIC Cocktails

The above experiments independently identified a series of CUBIC chemicals with high performance for delipidation, decoloring, RI matching, and decalcification. Because the requisite chemical properties for tissue clearing differ depending on the nature of the sample (e.g., lipid content, FP expression, existence of bone tissue), we sought to develop representative CUBIC cocktails that cover existing clearing demands. We began by developing two kinds of delipidation and decoloring cocktails, representing upgrades of Sca/eCUBIC-1: one for FP-compatible rapid delipidation and decoloring (CUBIC-L) and another for very rapid delipidation and decoloring (CUBIC-HL). According to our screening results, *N*-butyldiethanolamine and 1,3-bis(aminomethyl)cyclohexane were chosen for the main components of CUBIC-L and CUBIC-HL, respectively, because they had both high lipid solubility and decoloring scores. The combinatorial evaluation of detergents was performed using biological tissues. Since it is difficult to distinguish the clearing performance of individual cocktails under a long incubation time, we applied *N*-butyldiethanolamine-based cocktails to mouse brain and kidney and to human brain with a brief incubation (Figures 4A and S3A). The cocktail of *N*-butyldiethanolamine and Triton X-100 (termed CUBIC-L) exhibited the highest clearing ability for all of the specimens. The delipidation efficiency of all of the tested solutions was comparable in mouse brain and kidney, while anionic detergent-based cocktails (SDS, CU#0631 [sodium dodecylbenzenesulfonate], and CU#0865 [sodium nonanoate]) exhibited slightly higher

efficiencies than other solutions in human brain (Figure 4B). Notably, the tissue transparency of CUBIC-L was superior to that of other anionic detergent-based cocktails.

Sodium dodecylbenzenesulfonate (CU#0631) was an optimal cocktail for clearing human brain and kidney among the 1,3-bis(aminomethyl)cyclohexane-based cocktails (Figures 4C, 4D, and S3H). The cocktail of 1,3-bis(aminomethyl)cyclohexane and sodium dodecylbenzenesulfonate (CU#0631) (CUBIC-HL) achieved almost full delipidation. Next, we sought to optimize the RI-matching medium, an upgrade of Sca/eCUBIC-2, based on *N*-methylnicotinamide (CU#1283). Combinatorial experiments revealed that the cocktails of *N*-methylnicotinamide (CU#1283)-Histodenz and CU#1283-antipyrine showed much higher clearing performance than the single chemical solutions and other *N*-methylnicotinamide (CU#1283)-based cocktails (Figures 4E and S3F). In terms of cost efficiency, we chose the cocktail containing 30 wt% *N*-methylnicotinamide (CU#1283) and 45 wt% antipyrine as the RI-matching medium (CUBIC-RA). The even less expensive nicotinamide (CU#0855), a demethylated derivative of CU#1283, served as a convenient surrogate for *N*-methylnicotinamide (CU#1283) in combination with antipyrine; this cocktail was named CUBIC-R (Figure S3B).

We previously reported that a transient perfusion of Sca/eCUBIC-1 effectively cleared whole-body samples (Susaki et al., 2015; Tainaka et al., 2014). For this purpose, we introduced an optional CUBIC-L-based perfusion cocktail that included the decoloring-effective 1-methylimidazole, named CUBIC-P. To achieve efficient decalcification compatible with whole-body clearing, we chose the cocktail of 10 wt% EDTA and 15 wt% imidazole, named CUBIC-B. The proposed CUBIC cocktails except CUBIC-HL sufficiently preserved the fluorescent signal of mCherry (Figure 4F). CUBIC-RA is more feasible for various FPs such as EGFP and yellow fluorescent protein (YFP) than CUBIC-R (Figure S3E). These series of CUBIC cocktails are summarized in Figure 4G (original CUBIC protocol in Figure S3G), and four CUBIC protocols sequentially combining these cocktails are summarized in Figure 4H. By applying the protocols to a variety of tissue samples, including large human tissues, we demonstrated the effects of the updated CUBIC protocols (Figures 4I–4N, S3C, S3D, and S3I).

Figure 4. Combinatorial Screening of CUBIC Chemicals for Rapid and Scalable Tissue-Clearing CUBIC Protocols

(A) Combinatorial screening of delipidation chemicals compatible with FP. CU#0414 was mixed with various detergents. Mouse brain hemispheres, kidneys, and human brain blocks were delipidated with individual chemical cocktails and were then immersed in CUBIC-R.

(B) Phospholipid content of the tested biological tissues treated with CU#0414-based delipidation cocktails (n = 3).

(C) Combinatorial screening of delipidation chemicals for human brain and kidney blocks. 1,3-bis(aminomethyl)cyclohexane (CU#0070) was mixed with various detergents.

(D) Phospholipid content of human brain blocks treated with CU#0070-based delipidation cocktails. The CU#0070-CU#1455 cocktail precipitated (n = 3).

(E) Combinatorial screening of RI matching reagents. Delipidated adult (8-week-old) mouse lungs were immersed in highly concentrated chemical cocktails. RI of the mixtures is shown in blue.

(F) Time course of fluorescent signals from mCherry with each CUBIC cocktail (n = 3).

(G and H) Chemical components in CUBIC cocktails (G), and CUBIC protocols using serial treatments with CUBIC cocktails (H).

(I) Clearing performance of CUBIC protocol I for adult (6-week-old) mouse brain and kidney.

(J–L) Clearing performance of CUBIC protocol II for adult (8-week-old) mouse leg (J), P7 mouse head and body (K), and adult (8-week-old) mouse spinal cord (L4–L6) (L). Grids were visible through hard bone tissue (red arrows, K).

(M) Clearing performance of CUBIC protocol III for human heart and kidney blocks.

(N) Clearing performance of CUBIC protocol IV for human brain block.

Scale bars indicate 4 mm. Data are means ± SDs. See also Figure S3.

Inspection of the Tissue Integrity of CUBIC-Treated Organs

To demonstrate how the CUBIC protocols could outperform other clearing methods, we compared CUBIC protocol I with previously reported clearing methods. The final clearing performance of the CUBIC protocols was significantly better than that of other protocols (Figure S4). The updated CUBIC protocol also improved the imaging quality at deeper regions of the sample (Figure 5A). Since tissue clearing is often accompanied by macroscale tissue deformation, we also examined the effect of clearing on the brain macroshape. Because the final morphology of tissues was influenced by the pH of CUBIC-R, we tested both neutral and weakly basic CUBIC-Rs. The neutral CUBIC-R showed little deformation, while the weakly basic CUBIC-R exhibited swelling (Figure 5B). In addition, a cleared mouse brain (CUBIC protocol I) showed preserved subcellular microstructures (Figure 5C). To evaluate protein loss during the clearing process, we quantified the amount of residual protein after a 4-day delipidation using human brain tissue. Most of the endogenous protein was retained in the brain after CUBIC delipidation, even using the harshest CUBIC-HL protocol (Figure S4D). We also tested the antigenicity of delipidated mouse brain by immunohistochemistry using anti-glial fibrillary acidic protein (GFAP) and anti-NeuN antibodies and found that the antigenicity was preserved after a 4-day CUBIC-HL treatment (Figure 5D). In addition, using various antibodies on delipidated human brain, we observed that the antigenicity remained unaltered after a 9-day CUBIC-L treatment (Figure 5E). We further demonstrated the applicability of the protocols for 3D staining using lectin and an anti-smooth muscle actin (SMA) antibody on CUBIC-L delipidated human brain (Figure 5F). These findings indicated that the proposed protocols largely retain the amount and antigenicity of the proteins. We also applied our CUBIC protocols to comprehensive cell analysis at the whole-organ scale (Figure S5). The application of the CUBIC protocol I revealed comprehensive segmentation of the glomeruli in a mouse kidney (Figures S5A–S5E) and whole-organ cell detection in the left medial lobe of the liver and left lung of a mouse (Figures S5F–S5M).

Scalable Imaging of Mouse Whole Body, Including the Inside of Bone, and Large Human Organ Blocks by CUBIC Protocols

To perform exhaustive whole-body imaging, we applied CUBIC protocol II to render transparent the whole body of a P7 mouse and stained it with nuclear-staining dye (Figure 6A; Video S1). The volume rendered whole-body image showed strong fluorescence inside bones, as seen in the densely concentrated cells in the bone marrow (Figure 6B). CUBIC protocol II enabled brain and spine imaging at single-cell resolution in the skull and backbone (Figures 6C, 6D, S6A, and S6B). The imaging was even possible with adult mouse head and spine (Figures S6C–S6H). Next, we applied this protocol to metastatic bone tumors in the leg of an MDA-231-D-injected mouse (Figures 6E–6H and S6I) and observed the infiltration of metastatic cancer cells from bone tissue to the adjacent soft tissues. The metastatic bone tumors were even visible through skull (Figures S6J and S6K).

To examine the scalability of the CUBIC protocols, we applied CUBIC protocol III to large human tissue blocks; a large chunk of dissected human lung (approximately $43.4 \times 16.0 \times 26.4 \text{ mm}^3$; Figure S6L; Video S2), dissected human kidneys (Figure S6N), and a dissected human liver. Using light-sheet fluorescence microscopy (LSFM), multidirectional imaging was performed to acquire autofluorescence images throughout the blocks. We confirmed that the fluorescent signal was sufficient for imaging even deep within the blocks (Figures 6I, S6M, and S6O–S6Q). To examine the feasibility of volumetric imaging of human kidney at single-cell resolution, we visualized the 3D structure of the glomerulus after nuclear staining. Confocal imaging of the highly cleared tissue enabled the identification and segmentation of glomeruli in the magnified view (Figure 6J) and even the comprehensive detection of glomerular cells in the magnified view (Figures 6K and 6L).

We next performed the whole-brain imaging of an adult marmoset. The brain of a 1-year-old male marmoset was cleared using a modified CUBIC protocol I with *propidium iodide* (PI) staining, resulting in a cleared PI-stained brain without apparent morphological distortion (Figure S6R). The whole-brain images were acquired with LSFM and subjected to 3D image reconstruction to generate a volume-rendered image (Figures 6M and 6N; Video S3). Individual cells were distinguishable even in the deep regions of the brain (Figure 6O).

Multiple Visualization of Transgenically Labeled FPs in Mouse Brain

Simple immersion-based CUBIC protocols should be applicable and highly reproducible for tissue clearing without the significant quenching of FPs. We next used CUBIC protocol I combined with the visualization of a series of fluorescently labeled mouse samples. We prepared mouse brains with a wide variety of genetically encoded FPs (Thy1-YFP [Feng et al., 2000], P(CAG)-EGFP [Okabe et al., 1997], Drd1-mVenus [Nagai et al., 2016], Th-EGFP [Matsushita et al., 2002], Mcl1-YFP [Mlc1-tTA (Tanaka et al., 2010)::tetO-YC (Kanemaru et al., 2014)], Plp-YFP [Plp-tTA (Inamura et al., 2012)::tetO-ChR2EYFP (Tanaka et al., 2012)], and Htr5b-YFP [Htr5b-tTA (Tanaka et al., 2012)::tetO-YC]). The brain samples were subjected to CUBIC protocol I, with CUBIC-RA as an RI matching reagent to preserve the FP signals. All of the brains were treated with a nuclear staining dye (RedDot2) for registration, and images were acquired with LSFM, resulting in two volumetric images (one for the nuclear stain and the other for the FP signal) for each brain. We registered the nuclear images to that of a reference brain, and directly compared the FP signals by overlaying their registered images, as we reported previously (Susaki et al., 2014, 2015), thus achieving virtual multiplex whole-brain imaging (Figures 7A, S7A, and S7B). The overlaid image made it possible to compare the global distribution of pyramidal neurons (Thy1-YFP), astrocytes (Mlc1-YFP), oligodendrocytes (Plp-YFP), dopaminergic neurons (Th-EGFP), serotonin receptor 5B (Htr5b-YFP), and dopamine receptor D1 (Drd1-mVenus) at the whole-brain scale (Figures 7B and S7C; Video S4). This systematic approach to analyzing the global distribution of expressed genes enabled us to investigate the distribution of neural subtypes in the

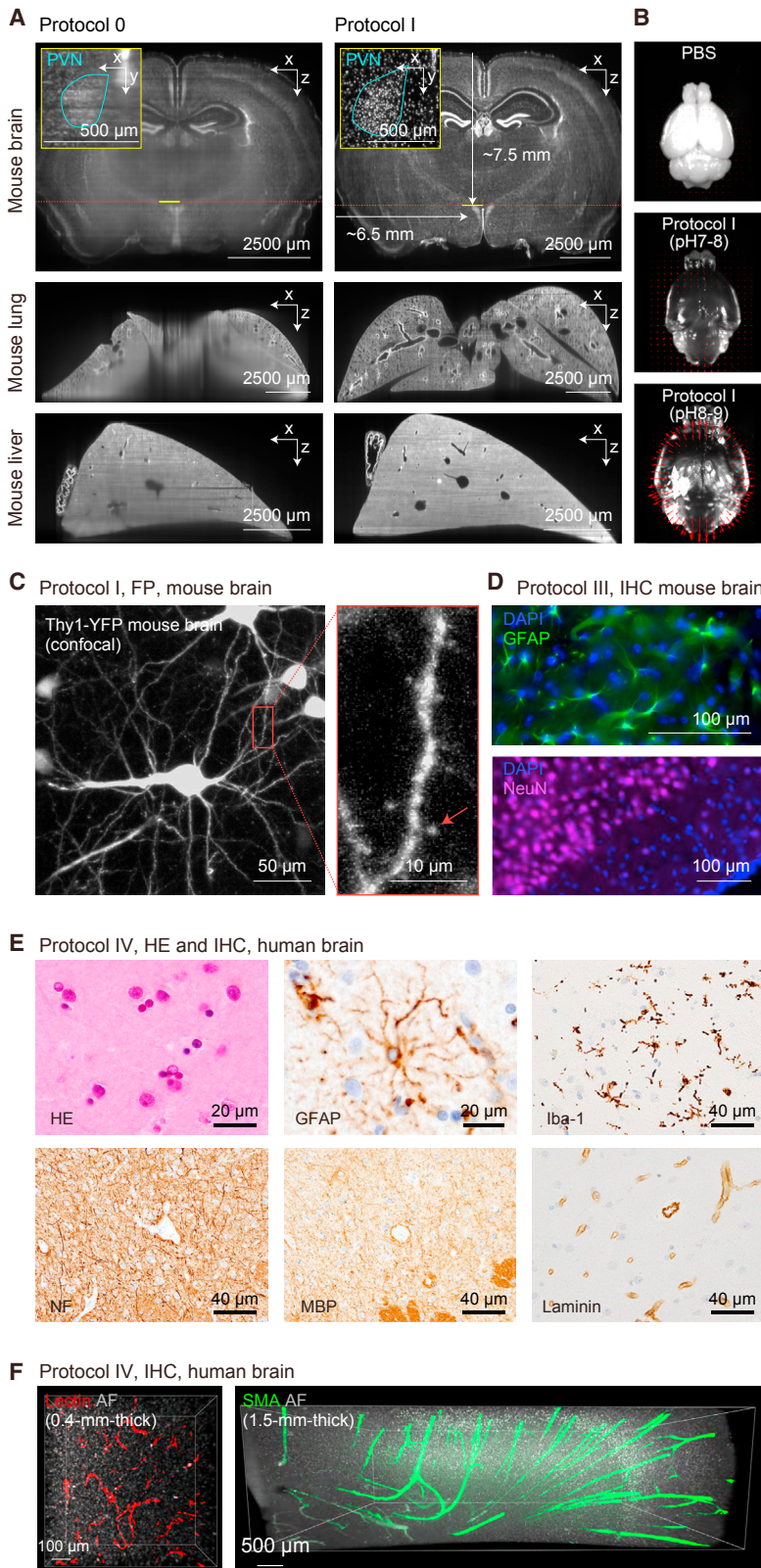


Figure 5. Tissue Integrity of CUBIC-Treated Organs

(A) LSFM images of nucleus-stained 8-week-old brain, lung, and left medial lobe of the liver after CUBIC protocol 0 and CUBIC protocol I. To compare the image qualities fairly, imaging was performed only from one side of the tissue. x indicates the illumination direction and z indicates the detection direction of the LSFM. For brain, the hypothalamic nuclei of paraventricular nuclei (PVN) are visualized in the insets. The scales for CUBIC protocols 0 and I were slightly adjusted to correct for shrinkage caused by CUBIC protocol 0.

(B) Deformation analysis of cleared 8-week-old mouse brains using CUBIC protocol I. The cleared brains were registered to a standard brain, and then the deformation fields were visualized on the projection images of the brains. In the RI-matching step, neutral CUBIC-R (without #0414; middle) and basic CUBIC-R (pH 8–9 adjusted with CU#0414; bottom) were applied; see also [STAR Methods](#) for details.

(C) Subcellular imaging of a 6-month-old Thy1-YFP mouse brain after CUBIC protocol I. A cellular view (left) and a magnified view (right) are shown. A representative spine is indicated by a red arrow (right).

(D) Immunohistochemistry of an 8-week-old mouse brain after a 4-day CUBIC-HL treatment. Anti-GFAP (top) and anti-NeuN (bottom) antibodies were used.

(E) H&E (HE) staining (top left) and immunohistochemistry of human brain after CUBIC protocol IV. Antibodies for glial fibrillary acidic protein (GFAP), ionized calcium-binding adaptor molecule 1 (Iba-1), neurofilament (NF), myelin basic protein (MBP), and laminin were examined.

(F) Visualization of vascular structures in thick slices of a human brain. Lectin (for 0.4-mm-thick brain slice; left) and anti- α -SMA antibody (for 1.5-mm-thick slice; right) were applied. The 3D volumetric images were obtained with LSFM.

See also [Figures S4](#) and [S5](#).

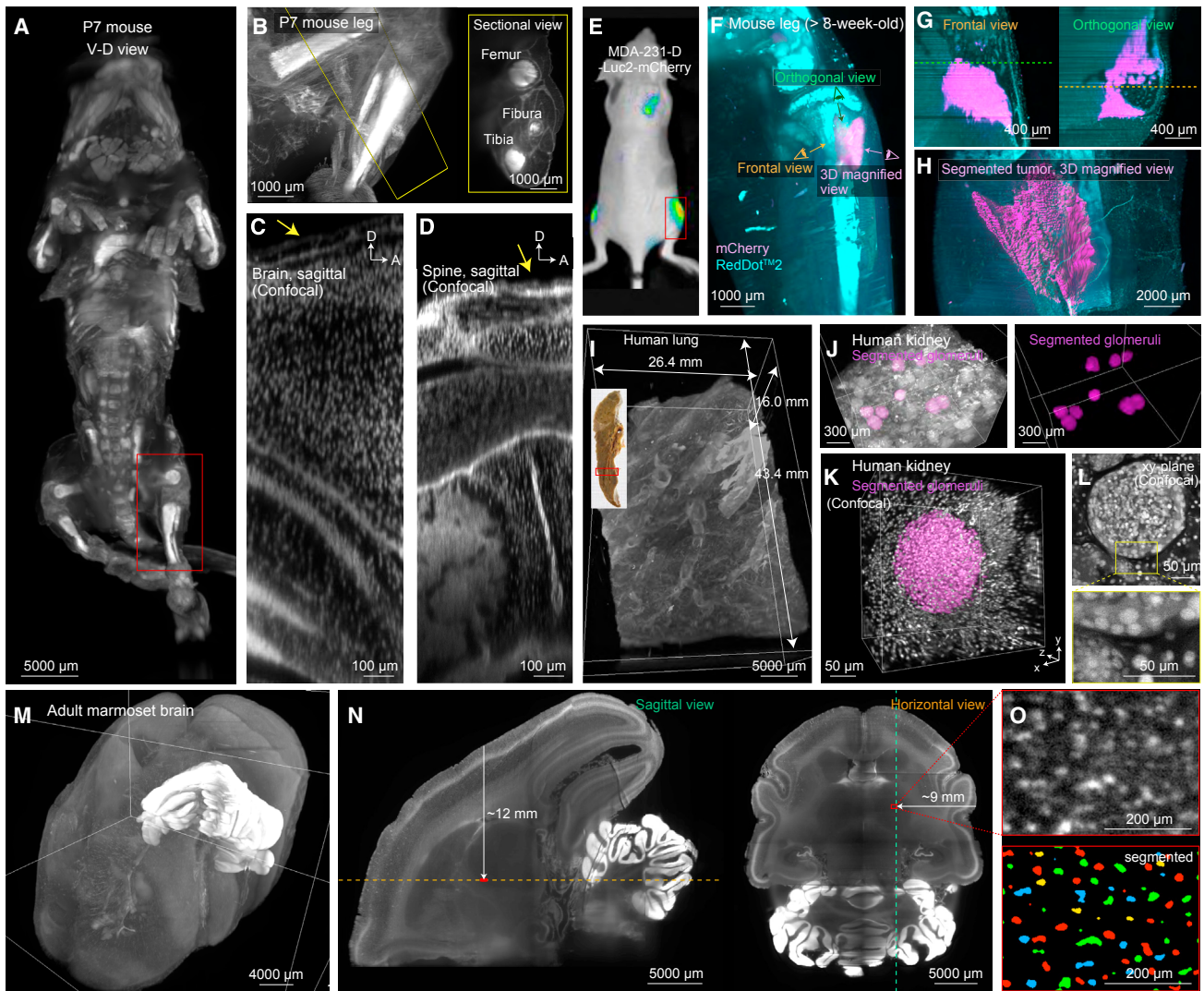


Figure 6. Scalable Imaging of Mouse Whole Body, Including Bone, and of Large Human Tissue Blocks with Single-Cell Resolution

(A and B) Volume-rendered images of whole mouse body (P7) stained with nuclear-staining dye. Ventral-dorsal whole-body view (A) and magnified view of left leg (B). Inset of (B), sectional view of the leg. CUBIC protocol II was applied.

(C and D) Confocal images of the brain inside the skull in a sagittal plane (C) and of the spine in a sagittal plane (D). Yellow arrows indicate bone tissues.

(E) Bioluminescence image of an MDA-231-D-injected immunodeficient BALB/c-nu/nu mouse.

(F) Volume-rendered image of the right leg of the mouse in (E). Magenta and cyan indicate metastasized cancer cells (mCherry) and nuclei (RedDot2), respectively. (G and H) Frontal (G, left), orthogonal (G, right), and magnified (H) views of (F). For (H), the segmented metastatic colony was visualized. For (F)–(H), CUBIC protocol II was applied.

(I) Volume-rendered image of the autofluorescence in a dissected human lung. CUBIC protocol III was applied.

(J) Volume-rendered image of nuclear-stained human kidney. Several glomeruli were segmented and are shown at right. CUBIC protocol III was applied.

(K and L) Confocal imaging of a single glomerulus in the human kidney. Volume-rendered image (K, top) and magnified single-cell-resolution view of the sectional image (L, bottom).

(M–O) Adult marmoset brain stained for nuclei. Volume-rendered image of whole brain (M), sectional views (N), and highly resolved images (O). All images acquired with LSFM. Modified CUBIC protocol I was applied (STAR Methods). See also Figure S6.

cerebral cortical layers (Figures 7C, 7D, and S7D). *In utero* electroporation is another method for introducing an exogenous gene. We unilaterally introduced P(CAG)::mRFP (monomeric red fluorescent protein) into mouse brain by *in utero* electroporation (Hayashi-Takagi et al., 2015) and analyzed the spatial distribution of the induced genes by virtual multi-

plex whole-brain imaging; this demonstrated that the mRFPs were mainly expressed into layer 4 (Figures 7E–7G). Furthermore, FP expressed in metastatic tumor cells (MDA-231-D cancer cells expressing mCherry) was also clearly visible using our CUBIC protocol I, allowing the morphological analysis of cancer metastasis (Figure 7H).

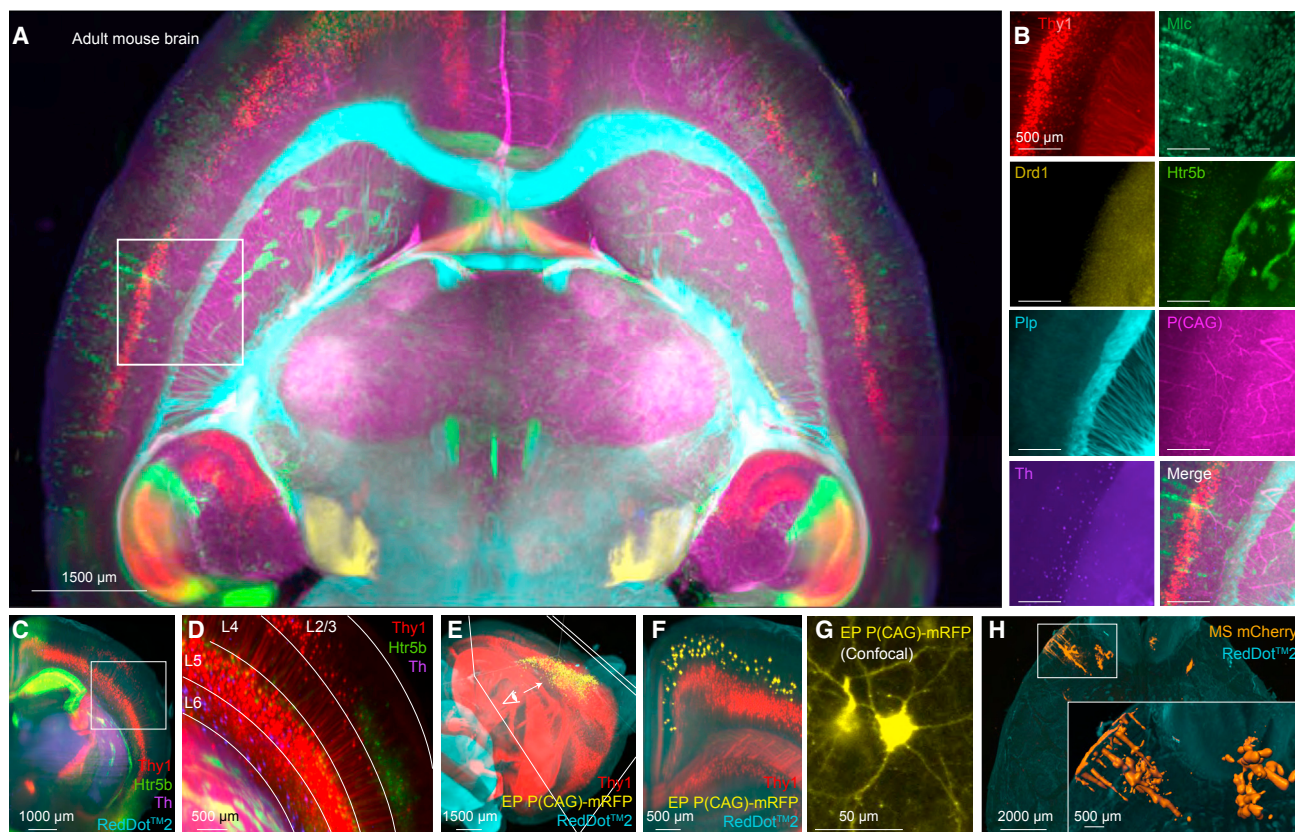


Figure 7. Multiple Visualization of Transgenically Labeled FPs in Mammalian Brains and Scalable Imaging of Brains with Single-Cell Resolution

(A–D) Virtual multiplex images of FP-expressing mouse brains registered to a standard brain. Overlaid images of seven different FPs (horizontal view; 300- μ m-thick projection) (A). Individual expression patterns and merged images in magnified views of the indicated region of (A) (B). Overlaid images of three different FPs (coronal view; 300- μ m-thick projection) (C) and magnified view of the indicated region of (C) (D). Cortical layer structures are indicated in (D).

(E and F) Multiplex images of mouse brain labeled with EP-induced mRFP overlaid with Thy1 and nuclear images. Volumetric image (E) and coronal view of the 300- μ m-thick projection in (E) and (F).

(G) Subcellular resolution imaging of mRFP-expressing cells by confocal microscopy.

(H) Metastasized colonies of MDA-231-D cells expressing mCherry (MS mCherry) in mouse brain; volumetric image overlaid with nuclear image. Inset shows segmented volumes of cancer metastasis.

For (A)–(H), CUBIC protocol I was applied. See also [Figure S7](#) and [STAR Methods](#).

DISCUSSION

Here, by applying comprehensive chemical profiling for delipidation, decoloring, RI matching, and decalcification, we designed a set of chemical tools for tissue clearing. Organic salts had poor efficiencies for delipidation and decoloring ([Figures S2A and S2F](#)). The undesirable effect of ionic charge in these steps was probably related to its effect on the molecular flux between a tissue and the external medium ([Hama et al., 2011; Hou et al., 2015](#)). Deionization by an osmotic-pressure gradient is a straightforward way to increase molecular flux; therefore, non-ionic cocktails that promoted molecular flux were advantageous in these steps. Detergents also had unexpectedly poor efficiencies for the delipidation and decoloring of tissue samples, given their high scores in the *in vitro* assay ([Figures 2F, 2H, S2A, and S2F](#)). Tissue delipidation and decoloring using detergents is often achieved by combining them with other tissue-

permeable chemicals ([Hama et al., 2015; Susaki et al., 2014](#)) or with chemophysical assistance ([Chung et al., 2013; Murray et al., 2015; Tainaka et al., 2014; Yang et al., 2014](#)). Detergents generally show slow tissue-permeation kinetics as a result of large micelle formation, which could explain their poor efficiency in tissue. In contrast, amine derivatives with higher logP values are expected to be more cell permeable and more miscible with hydrophobic lipids. Among the current decoloring reagents, *N*-alkylimidazole showed the highest decoloring ability. *N*-Alkylimidazole facilitates heme elution under basic conditions by competing with histidine for binding to the heme iron center.

In the RI-matching step, an external medium with a high RI value similar to that of endogenous proteins ($RI \geq 1.45$) replaces the low-RI water ($RI = 1.33$) inside tissue. The final tissue transparency improves as the RI value of the medium increases (up to 1.52) under a given chemical composition ([Kubota et al., 2017](#)). Organic solvent-based RI media have high RI values

(e.g., benzyl alcohol/benzyl benzoate [BABB], 1.56; dibenzyl ether [DBE], 1.56). Our chemical profiling demonstrated that aromatic groups have high RI values because of their high electron density (Figure 3A). Thus, an aromatic derivative is likely to be a suitable constituent of RI media. In addition, the tissue clearing performance in a variety of RI media demonstrated that the final transparency was determined not only by the RI value but also by the chemical nature of the components of the RI medium (Figures 3C and 3E). Among the clearing protocols, sugar-based RI medium (e.g., see deep brain [SeeDB, Ke et al., 2013] and ScaleCUBIC-2) elicits moderate clearing compared with RI media consisting of contrast reagents (e.g., CLARITY, refractive index matching solution [RIMS], SeeDB2 [Ke et al., 2016], and SWITCH). The effectiveness of antipyrine and nicotinamide in our screen indicated that the high clearing efficiency of contrast reagents is derived from their aromatic amide group. Since highly delipidated tissues are regarded as protein-based biomaterials (Murakami et al., 2018), it is plausible that hydrophilic aromatic amides contributed to RI homogenization because of their efficient solvation of protein backbone amides. A future strategy for improving RI media will be to explore chemical combinations that promote the solvation of the major proteins in tissues.

Our updated protocols have a few potential limitations. Since both of the delipidation cocktails are alkaline-buffered solutions, almost all of the endogenous RNA would be degraded. To perform RNA profiling, a 1,2-hexanediol-based delipidation cocktail needs to be developed. In addition, much of the presynaptic and post-synaptic fabric is reported to disappear with thorough delipidation protocols such as 3D imaging of solvent-cleared organs (3DISCO), PACT, and the original ScaleCUBIC (Hama et al., 2015). Therefore, our protocols would be not suitable for the observation of these structures by electron microscopy. Furthermore, while our decoloring reagents are effective for bleaching porphyrin-related pigments such as myoglobin and cytochrome c, they are unlikely to affect melanin, which is formed by the oxidative polymerization of amino acids (Sealy et al., 1980). Another decoloring strategy is needed to bleach such polymerized pigments.

In summary, we applied comprehensive chemical profiling as a rational design strategy for obtaining purposeful clearing cocktails. A visual guide for this design strategy is shown in Figure S8. The application of these protocols should contribute to a rich variety of studies, including the prospective atlas of human cells.

STAR★METHODS

Detailed methods are provided in the online version of this paper and include the following:

- **KEY RESOURCES TABLE**
- **CONTACT FOR REAGENT AND RESOURCE SHARING**
- **EXPERIMENTAL MODEL AND SUBJECT DETAILS**
 - Marmoset
 - Mice Model
 - Human Tissue
- **METHOD DETAILS**
 - High-throughput Chemical Screening
 - Chemical Parameters

- Multivariate Linear Regression Analysis
- CUBIC Protocols
- Deformation Analysis of Cleared Brains
- Long-term Tissue Preservation
- Immunostaining
- Microscopy
- *In Vivo* Bioluminescence Imaging
- Histological Examination
- Image Analysis
- **QUANTIFICATION AND STATISTICAL ANALYSIS**
 - Protein Quantification
 - Quantification of Image Quality
 - Statistical Analysis
- **DATA AND SOFTWARE AVAILABILITY**

SUPPLEMENTAL INFORMATION

Supplemental Information includes eight figures, two tables, and four videos and can be found with this article online at <https://doi.org/10.1016/j.celrep.2018.07.056>.

ACKNOWLEDGMENTS

We thank all of the laboratory members at The University of Tokyo and RIKEN Quantitative Biology Center (QBiC), in particular, K. Yoshida for help with the polynomial regression; S. Shi, G.A. Sunagawa, and R.G. Yamada for statistical analysis; and R. Ohno for housing mice. We also thank Y. Morishita and T. Tanda for histological analysis, S. Ehata and J. Nishida for experimental design of the metastasis model, H. Nawa and H. Namba for helping to prepare the Th-EGFP mouse brain, T. Mano for reproducing the image processing pipeline, Tokyo Chemical Industry for the CUBIC chemical library, Olympus Engineering for helping with the microscope design, and Bitplane for instruction in Imaris 8.1.2. This work was supported by grants from AMED-CREST (AMED/MEXT to H.R.U.) and CREST (JST/MEXT to H.R.U. and JPMJCR1652 to H.K.); PRESTO from JST(JPMJPR15F4 to E.A.S.); Brain/MINDS (AMED/MEXT to H.R.U.); the Basic Science and Platform Technology Program for Innovative Biological Medicine (AMED/MEXT to H.R.U.); the Japanese Initiative for Progress of Research on Infectious Disease for Global Epidemic (AMED, JP17fm0208023 to M.M. and K. Tainaka); Strategic Research Program from Brain Sciences (AMED, JP18dm0107120 to H.K.); Grant-in-Aid for Challenging Exploratory Research (JSPS KAKENHI grant 16K15124 to K. Tainaka); Grant-in-Aid for Young Scientists (A) (JSPS KAKENHI grant no. 15H05650 to E.A.S.); Grant-in-Aid for Scientific Research (JSPS KAKENHI grant no. 16J05041 to T.C.M.); Grant-in-Aid for Scientific Research (S) (JSPS KAKENHI grant no. 25221004 and 18H05270 to H.R.U. and 26221001 to H.K.); Grant-in-Aid for Scientific Research (B) (JSPS KAKENHI grant no. 18H02105 to K. Tainaka and 18H02540 to T.S. and K. Tainaka); Grants-in-Aid for Scientific Research on Innovative Areas (KAKENHI grant no. 23115006 to H.R.U. and 17H05688 and 18H04543 to K. Tainaka, and 17H06328 to E.A.S.) from MEXT; Grant-in-Aid from the Naito Science & Engineering Foundation (K. Tainaka); Grant-in-Aid from the Tokyo Biochemical Research Foundation (K. Tainaka); Grant-in-Aid from the Cell Science Research Foundation (K. Tainaka); Grant-in-Aid from the NOVARTIS Foundation (Japan) for the Promotion of Science (K. Tainaka); Grant-in-Aid from the Takeda Science Foundation (H.R.U. and E.A.S.); and grant from the Brain Sciences Project of the Center for Novel Science Initiatives of the National Institutes of Natural Sciences (BS291001 to E.A.S.).

AUTHOR CONTRIBUTIONS

H.R.U., K. Tainaka, and T.C.M. designed the study. K. Tainaka, T.C.M., and C.S. performed most of the experiments. K. Tainaka performed the chemical profiling for tissue clearing. T.C.M. performed the computational image

analysis. E.A.S. developed the modified CUBIC protocol for marmoset brain and performed LSFM imaging of the marmoset brain. R.S. and A.K. prepared human brain tissues and performed the clearing and LSFM imaging of human brain tissues. S.N., M. Ikemura, T.U., E.M., and M.F. prepared human tissues. T.I. housed the marmosets and prepared marmoset brains. K. Takahashi and K.M. produced the experimental metastatic model. A.H.-T. and H.K. produced exogenously FP-labeled mice by *in utero* electroporation. Y.S. produced the recombinant fluorescent proteins. H.S., Y.A., K.F.T., M. Iino, M.M., T.S., and K.K. housed a series of mice used in this study and prepared organ samples. H.R.U., K. Tainaka, and T.C.M. wrote the manuscript. All of the authors discussed the results and commented on the manuscript text.

DECLARATION OF INTERESTS

The RIKEN Quantitative Biology Center has filed a patent based on this work in which T.C.M., K. Tainaka, and H.R.U. are co-inventors. Part of this study was done in collaboration with Olympus Corporation.

Received: January 31, 2018

Revised: May 21, 2018

Accepted: July 15, 2018

Published: August 21, 2018

REFERENCES

- Ando, K., Laborde, Q., Lazar, A., Godefroy, D., Youssef, I., Amar, M., Pooler, A., Potier, M.-C., Delatour, B., and Duyckaerts, C. (2014). Inside Alzheimer brain with CLARITY: senile plaques, neurofibrillary tangles and axons in 3-D. *Acta Neuropathol.* **128**, 457–459.
- Avants, B.B., Tustison, N.J., Song, G., Cook, P.A., Klein, A., and Gee, J.C. (2011). A reproducible evaluation of ANTs similarity metric performance in brain image registration. *Neuroimage* **54**, 2033–2044.
- Becker, K., Jährling, N., Saghaei, S., Weiler, R., and Dodt, H.U. (2012). Chemical clearing and dehydration of GFP expressing mouse brains. *PLoS One* **7**, e33916.
- Belle, M., Godefroy, D., Dominici, C., Heitz-Marchaland, C., Zelina, P., Hellal, F., Bradke, F., and Chédotal, A. (2014). A simple method for 3D analysis of immunolabeled axonal tracts in a transparent nervous system. *Cell Rep.* **9**, 1191–1201.
- Belle, M., Godefroy, D., Couly, G., Malone, S.A., Collier, F., Giacobini, P., and Chédotal, A. (2017). Tridimensional visualization and analysis of early human development. *Cell* **169**, 161–173.e12.
- Chung, K., Wallace, J., Kim, S.Y., Kalyanasundaram, S., Andalman, A.S., Davidson, T.J., Mirzabekov, J.J., Zalocusky, K.A., Mattis, J., Denisin, A.K., et al. (2013). Structural and molecular interrogation of intact biological systems. *Nature* **497**, 332–337.
- Doerr, J., Schwarz, M.K., Wiedermann, D., Leinhaas, A., Jakobs, A., Schloen, F., Schwarz, I., Diedenhofen, M., Braun, N.C., Koch, P., et al. (2017). Whole-brain 3D mapping of human neural transplant innervation. *Nat. Commun.* **8**, 14162.
- Ehata, S., Hanyu, A., Fujime, M., Katsuno, Y., Fukunaga, E., Goto, K., Ishikawa, Y., Nomura, K., Yokoo, H., Shimizu, T., et al. (2007). Ki26894, a novel transforming growth factor- β type I receptor kinase inhibitor, inhibits *in vitro* invasion and *in vivo* bone metastasis of a human breast cancer cell line. *Cancer Sci.* **98**, 127–133.
- Feng, G., Mellor, R.H., Bernstein, M., Keller-Peck, C., Nguyen, Q.T., Wallace, M., Nerbonne, J.M., Lichtman, J.W., and Sanes, J.R. (2000). Imaging neuronal subsets in transgenic mice expressing multiple spectral variants of GFP. *Neuron* **28**, 41–51.
- Gao, L. (2015). Extend the field of view of selective plan illumination microscopy by tiling the excitation light sheet. *Opt. Express* **23**, 6102–6111.
- Hama, H., Kurokawa, H., Kawano, H., Ando, R., Shimogori, T., Noda, H., Fukami, K., Sakaue-Sawano, A., and Miyawaki, A. (2011). *Scale*: a chemical approach for fluorescence imaging and reconstruction of transparent mouse brain. *Nat. Neurosci.* **14**, 1481–1488.
- Hama, H., Hioki, H., Namiki, K., Hoshida, T., Kurokawa, H., Ishidate, F., Kaneko, T., Akagi, T., Saito, T., Saido, T., and Miyawaki, A. (2015). *ScaleS*: an optical clearing palette for biological imaging. *Nat. Neurosci.* **18**, 1518–1529.
- Hansen, C.M. (2007). *Hansen Solubility Parameters: A User's Handbook* (CRC Press).
- Harris, D.C. (2011). *Quantitative Chemical Analysis, Eighth Edition* (W. H. Freeman).
- Hayashi-Takagi, A., Yagishita, S., Nakamura, M., Shirai, F., Wu, Y.I., Loshbaugh, A.L., Kuhlman, B., Hahn, K.M., and Kasai, H. (2015). Labelling and optical erasure of synaptic memory traces in the motor cortex. *Nature* **525**, 333–338.
- Hoshino, Y., Nishida, J., Katsuno, Y., Koinuma, D., Aoki, T., Kokudo, N., Miyazono, K., and Ehata, S. (2015). Smad4 decreases the population of pancreatic cancer-initiating cells through transcriptional repression of ALDH1A1. *Am. J. Pathol.* **185**, 1457–1470.
- Hou, B., Zhang, D., Zhao, S., Wei, M., Yang, Z., Wang, S., Wang, J., Zhang, X., Liu, B., Fan, L., et al. (2015). Scalable and Dil-compatible optical clearance of the mammalian brain. *Front. Neuroanat.* **9**, 19.
- Inamura, N., Sugio, S., Macklin, W.B., Tomita, K., Tanaka, K.F., and Ikenaka, K. (2012). Gene induction in mature oligodendrocytes with a PLP-tTA mouse line. *Genesis* **50**, 424–428.
- Kanemaru, K., Sekiya, H., Xu, M., Satoh, K., Kitajima, N., Yoshida, K., Okubo, Y., Sasaki, T., Moritoh, S., Hasuwa, H., et al. (2014). *In vivo* visualization of subtle, transient, and local activity of astrocytes using an ultrasensitive Ca^{2+} indicator. *Cell Rep.* **8**, 311–318.
- Ke, M.-T., Fujimoto, S., and Imai, T. (2013). SeeDB: a simple and morphology-preserving optical clearing agent for neuronal circuit reconstruction. *Nat. Neurosci.* **16**, 1154–1161.
- Ke, M.-T., Nakai, Y., Fujimoto, S., Takayama, R., Yoshida, S., Kitajima, T.S., Sato, M., and Imai, T. (2016). Super-resolution mapping of neuronal circuitry with an index-optimized clearing agent. *Cell Rep.* **14**, 2718–2732.
- Kiviranta, I., Tammi, M., Lappalainen, R., Kuusela, T., and Helminen, H.J. (1980). The rate of calcium extraction during EDTA decalcification from thin bone slices as assessed with atomic absorption spectrophotometry. *Histochemistry* **68**, 119–127.
- Kubota, S.I., Takahashi, K., Nishida, J., Morishita, Y., Ehata, S., Tainaka, K., Miyazono, K., and Ueda, H.R. (2017). Whole-body profiling of cancer metastasis with single-cell resolution. *Cell Rep.* **20**, 236–250.
- Liebmann, T., Renier, N., Bettayeb, K., Greengard, P., Tessier-Lavigne, M., and Flajolet, M. (2016). Three-dimensional study of Alzheimer's disease hallmarks Using the iDISCO clearing method. *Cell Rep.* **16**, 1138–1152.
- Matsushita, N., Okada, H., Yasoshima, Y., Takahashi, K., Kiuchi, K., and Kobayashi, K. (2002). Dynamics of tyrosine hydroxylase promoter activity during midbrain dopaminergic neuron development. *J. Neurochem.* **82**, 295–304.
- Murakami, T.C., Mano, T., Saikawa, S., Horiguchi, S.A., Shigeta, D., Baba, K., Sekiya, H., Shimizu, Y., Tanaka, K.F., Kiyonari, H., et al. (2018). A three-dimensional single-cell-resolution whole-brain atlas using CUBIC-X expansion microscopy and tissue clearing. *Nat. Neurosci.* **21**, 625–637.
- Murray, E., Cho, J.H., Goodwin, D., Ku, T., Swaney, J., Kim, S.Y., Choi, H., Park, Y.G., Park, J.Y., Hubbert, A., et al. (2015). Simple, scalable proteomic imaging for high-dimensional profiling of intact systems. *Cell* **163**, 1500–1514.
- Nagai, T., Nakamuta, S., Kuroda, K., Nakauchi, S., Nishioka, T., Takano, T., Zhang, X., Tsuboi, D., Funahashi, Y., Nakano, T., et al. (2016). Phosphoproteomics of the dopamine pathway enables discovery of Rap1 activation as a reward signal *in vivo*. *Neuron* **89**, 550–565.
- Okabe, M., Ikawa, M., Kominami, K., Nakanishi, T., and Nishimune, Y. (1997). 'Green mice' as a source of ubiquitous green cells. *FEBS Lett.* **407**, 313–319.
- Pan, C., Cai, R., Quacquarelli, F.P., Ghasemigharagoz, A., Lourdopoulos, A., Matryba, P., Plesnila, N., Dichgans, M., Hellal, F., and Ertürk, A. (2016). Shrinkage-mediated imaging of entire organs and organisms using uDISCO. *Nat. Methods* **13**, 859–867.
- Preibisch, S., Saalfeld, S., and Tomancak, P. (2009). Globally optimal stitching of tiled 3D microscopic image acquisitions. *Bioinformatics* **25**, 1463–1465.

- Renier, N., Wu, Z., Simon, D.J., Yang, J., Ariel, P., and Tessier-Lavigne, M. (2014). iDISCO: a simple, rapid method to immunolabel large tissue samples for volume imaging. *Cell* **159**, 896–910.
- Renier, N., Adams, E.L., Kirst, C., Wu, Z., Azevedo, R., Kohl, J., Autry, A.E., Kadiri, L., Umadevi Venkataraju, K., Zhou, Y., et al. (2016). Mapping of brain activity by automated volume analysis of immediate early genes. *Cell* **165**, 1789–1802.
- Royer, L.A., Lemon, W.C., Chhetri, R.K., Wan, Y., Coleman, M., Myers, E.W., and Keller, P.J. (2016). Adaptive light-sheet microscopy for long-term, high-resolution imaging in living organisms. *Nat. Biotechnol.* **34**, 1267–1278.
- Santi, P.A., Johnson, S.B., Hillenbrand, M., GrandPre, P.Z., Glass, T.J., and Leger, J.R. (2009). Thin-sheet laser imaging microscopy for optical sectioning of thick tissues. *Biotechniques* **46**, 287–294.
- Schindelin, J., Arganda-Carreras, I., Frise, E., Kaynig, V., Longair, M., Pietzsch, T., Preibisch, S., Rueden, C., Saalfeld, S., Schmid, B., et al. (2012). Fiji: an open-source platform for biological-image analysis. *Nat. Methods* **9**, 676–682.
- Sealy, R.C., Felix, C.C., Hyde, J.S., and Swartz, H.M. (1980). Structure and reactivity of melanins: influence of free radicals and metal ions. In *Free Radicals in Biology*, W.A. Pryor, ed. (Academic Press), pp. 209–259.
- Serper, A., and Calt, S. (2002). The demineralizing effects of EDTA at different concentrations and pH. *J. Endod.* **28**, 501–502.
- Smith, R.M., Martell, A.E., and Motekaitis, R.J. (2003). NIST Standard Reference Database 46. Critically Selected Stability Constants of Metal Complexes Database (US National Institute of Standards and Technology Standard Reference Data Program), p. 20899.
- Spalteholz, W. (1914). *Über das Durchsichtigmachen von menschlichen und tierischen Präparaten* (S. Hirzel).
- Susaki, E.A., and Ueda, H.R. (2016). Whole-body and whole-organ clearing and imaging techniques with single-cell resolution: toward organism-level systems biology in mammals. *Cell Chem. Biol.* **23**, 137–157.
- Susaki, E.A., Tainaka, K., Perrin, D., Kishino, F., Tawara, T., Watanabe, T.M., Yokoyama, C., Onoe, H., Eguchi, M., Yamaguchi, S., et al. (2014). Whole-brain imaging with single-cell resolution using chemical cocktails and computational analysis. *Cell* **157**, 726–739.
- Susaki, E.A., Tainaka, K., Perrin, D., Yukinaga, H., Kuno, A., and Ueda, H.R. (2015). Advanced CUBIC protocols for whole-brain and whole-body clearing and imaging. *Nat. Protoc.* **10**, 1709–1727.
- Tainaka, K., Kubota, S.I., Suyama, T.Q., Susaki, E.A., Perrin, D., Ukai-Tadenuma, M., Ukai, H., and Ueda, H.R. (2014). Whole-body imaging with single-cell resolution by tissue decolorization. *Cell* **159**, 911–924.
- Tainaka, K., Kuno, A., Kubota, S.I., Murakami, T., and Ueda, H.R. (2016). Chemical principles in tissue clearing and staining protocols for whole-body cell profiling. *Annu. Rev. Cell Dev. Biol.* **32**, 713–741.
- Tanaka, K.F., Ahmari, S.E., Leonardo, E.D., Richardson-Jones, J.W., Budreck, E.C., Scheiffele, P., Sugio, S., Inamura, N., Ikenaka, K., and Hen, R. (2010). Flexible accelerated STOP tetracycline operator-knockin (FAST): a versatile and efficient new gene modulating system. *Biol. Psychiatry* **67**, 770–773.
- Tanaka, K.F., Matsui, K., Sasaki, T., Sano, H., Sugio, S., Fan, K., Hen, R., Nakai, J., Yanagawa, Y., Hasuwa, H., et al. (2012). Expanding the repertoire of optogenetically targeted cells with an enhanced gene expression system. *Cell Rep.* **2**, 397–406.
- Treweek, J.B., Chan, K.Y., Flytzanis, N.C., Yang, B., Deverman, B.E., Greenbaum, A., Lignell, A., Xiao, C., Cai, L., Ladinsky, M.S., et al. (2015). Whole-body tissue stabilization and selective extractions via tissue-hydrogel hybrids for high-resolution intact circuit mapping and phenotyping. *Nat. Protoc.* **10**, 1860–1896.
- Weast, R.C. (1983). *CRC Handbook of Chemistry and Physics, Sixty-Second Edition* (CRC Press).
- Yang, B., Treweek, J.B., Kulkarni, R.P., Deverman, B.E., Chen, C.K., Lubeck, E., Shah, S., Cai, L., and Gradinaru, V. (2014). Single-cell phenotyping within transparent intact tissue through whole-body clearing. *Cell* **158**, 945–958.
- Zhang, M., Wu, T., and Bennett, K.M. (2015). Small blob identification in medical images using regional features from optimum scale. *IEEE Trans. Biomed. Eng.* **62**, 1051–1062.

STAR★METHODS

KEY RESOURCES TABLE

REAGENT or RESOURCE	SOURCE	IDENTIFIER
Antibodies		
GFAP	Sigma-Aldrich	Cat#C9205; AB_476889
NeuN	Millipore	Cat#MAB377; AB_2149209
Donkey anti-mouse IgG	Thermo Fisher Scientific	Cat#A21203; AB_2535789
GFAP	Dako	Cat#Z0334; AB_10013382
Iba1	Wako	Cat#019-19741; AB_839504
Laminin	Dako	Cat#Z0097; AB_10013382
MBP	Dako	Cat#A0623; AB_2650566
NF	Monosan	Cat#MON3004; AB_2314914
α -SMA	Novus Biological	Cat#IC1420R
Lectin	Vector Laboratories	Cat#RL-1062
Biological Samples		
Horse blood	Kohjin-Bio	Cat#12070110
Chemicals, Peptides, and Recombinant Proteins		
Pentobarbital	Nacalai Tesque	Cat#02095-04
Paraformaldehyde	Nacalai Tesque	Cat#02890-45
Quadrol	Tokyo Chemical Industry	Cat#T0781
Triethanolamine	Wako Pure Chemical industries	Cat#145-05605
Triton X-100	Nacalai Tesque	Cat#12967-45
Urea	Nacalai Tesque	Cat#35904-45
Sucrose	Nacalai Tesque	Cat#30403-55
SDS	Nacalai Tesque	Cat#31606-75
Histodenz	Sigma-Aldrich	Cat#D2158
<i>N</i> -Butyldiethanolamine (CU#0414)	Tokyo Chemical Industry	Cat#B0725
1,3-Bis(aminomethyl)cyclohexane (cis- and trans- mixture) (CU#0070)	Tokyo Chemical Industry	Cat#B1005
1-Methylimidazole	Tokyo Chemical Industry	Cat#M0508
Antipyrine (CU#0640)	Tokyo Chemical Industry	Cat#D1876
<i>N</i> -Methylnicotinamide (CU#1283)	Tokyo Chemical Industry	Cat#M0374
Nicotinamide (CU#0855)	Tokyo Chemical Industry	Cat#N0078
EDTA	Tokyo Chemical Industry	Cat#E0084
Imidazole (CU#1352)	Tokyo Chemical Industry	Cat#I0001
Hydroxyapatite (HAp)	Sigma-Aldrich	Cat#289396
RedDot 2	Biotium	Cat#40061
Propidium iodide	Life Technologies	Cat#P21493
Agarose	Nacalai Tesque	Cat#01163-76
Silicon oil (RI = 1.555)	Shin-Etsu Chemical	Cat#HIVAC-F4
Mineral oil (RI = 1.467)	Sigma-Aldrich	Cat#M8410
CUBIC chemicals for screening	Tokyo Chemical Industry	Table S1
Critical Commercial Assays		
LabAssay Phospholipid	Wako Pure Chemical industries	Cat#296-63801
LabAssay Cholesterol	Wako Pure Chemical industries	Cat#296-65801
Microplate BCA Protein Assay Kit-Reducing Agent Compatible	Thermo Fisher Scientific	Cat#23252

(Continued on next page)

Continued

REAGENT or RESOURCE	SOURCE	IDENTIFIER
Experimental Models: Cell Lines		
MDA-MB-231-5a-D	Ehata et al., 2007	N/A
Experimental Models: Organisms/Strains		
Htr5b-tTA:tetO-YC	Tanaka et al., 2012 Kanemaru et al., 2014	N/A
Plp-tTA:tetO-ChR2EYFP	Inamura et al., 2012 Tanaka et al., 2012	N/A
Mlc-tTA:tetO-YC	Tanaka et al., 2010	N/A
DrD1-mVenus	Nagai et al., 2016	N/A
Th-EGFP	Matsushita et al., 2002	N/A
Thy1-YFP-H	Feng et al., 2000	N/A
P(CAG)-EGFP	Okabe et al., 1997	N/A
P(CAG)::mRFP	Hayashi-Takagi et al., 2015	N/A
Software and Algorithms		
Excel 2016	Microsoft	N/A
Origin 7.0	OriginLab	N/A
R	R Core Team	https://www.r-project.org
GraphPad Prism 5	GraphPad software	N/A
ChemDraw	Perkin Elmer	N/A
Fiji	Schindelin et al., 2012	https://fiji.sc/
Imaris	Bitplane	N/A
MATLAB	Mathworks	N/A
Customized MATLAB code for virtual multiplex imaging	This paper	https://github.com/DSP-sleep/Landscape_pipeline .

CONTACT FOR REAGENT AND RESOURCE SHARING

Further information and requests for resources and reagents should be directed to and will be fulfilled by the Lead Contact, Hiroki R. Ueda (uedah-ky@umin.ac.jp).

EXPERIMENTAL MODEL AND SUBJECT DETAILS

Marmoset

We studied an adult marmoset at the age of 12 months. Animal was maintained and handled in accordance with the recommendations of the United States National Institutes of Health, and all procedures were approved by the Animal Care and Use Committee of the Graduate School of Medicine, Kyoto University, Japan.

Mice Model

For the chemical screening ([Figures 1, 2, 3, 4](#) and [S1, S2, S3](#) and [Tables S1](#) and [S2](#)), the organs of adult mice (C57BL/6N, ICR, or BALB/c-nu/nu) were used. The mice were sacrificed by an overdose of pentobarbital (> 100 mg/kg, Nacalai Tesque, 02095-04), then transcardially perfused with 15 mL of PBS (pH 7.4) and 20 mL of 4% paraformaldehyde (PFA, Nacalai Tesque, 02890-45) in PBS. Organs were dissected, then post-fixed with 4% PFA-PBS at 4°C overnight. The fixed organs were then washed with PBS prior to the experiments.

The Htr5b-tTA ([Tanaka et al., 2012](#)):tetO-YC ([Kanemaru et al., 2014](#)) (7 weeks old), Plp-tTA ([Inamura et al., 2012](#)):tetO-ChR2EYFP ([Tanaka et al., 2012](#)) (10 weeks old), Mlc-tTA ([Tanaka et al., 2010](#)):tetO-YC (11 weeks old), Drd1-mVenus ([Nagai et al., 2016](#)) (7 months old), Th-EGFP ([Matsushita et al., 2002](#)) (6 months old), Thy1-YFP-H ([Feng et al., 2000](#)) (6 months old), and P(CAG)-EGFP ([Okabe et al., 1997](#)) (8 weeks old) mouse strains were used to observe the expression patterns of fluorescently labeled cells in the brain. P(CAG)::mRFP was transduced into mouse brain (8 weeks old) by in utero electroporation as described previously ([Hayashi-Takagi et al., 2015](#)).

The human breast cancer cells, MDA-MB-231-5a-D (MDA-231-D), are a highly metastatic clone derived from MDA-MB-231 ([Ehata et al., 2007](#)). We established MDA-231-D cells that co-expressed luciferase and mCherry according to our recent report ([Kubota et al., 2017](#)). To elicit experimental bone metastasis by intracardiac (i.c.) injection, MDA-231-D cells

(MDA-231-D: 1×10^5 cells/mouse) were injected into BALB/c-nu/nu mice (4-weeks old, female) by puncture into the left ventricle of heart. Mice were sacrificed 4 or 5 weeks after injection.

All experimental procedures and housing conditions were approved by the Animal Care and the Use Committee of the Graduate School of Medicine, University of Tokyo, and by the Animal Use and Care Committee of Niigata University, and all of the animals were cared for and treated humanely in accordance with the Institutional Guidelines for Experiments using animals.

Human Tissue

Human tissues used for this study were obtained from 10 patients (59–90 years old; 9 males and 1 female). Written informed consent for autopsy including the use of tissue for research purposes was obtained from the next of kin. Experiments using human tissues were approved by the institutional review boards of Osaka University School of Medicine, Osaka, Japan, the Graduate School of Medicine, University of Tokyo, Tokyo, Japan, and Niigata University School of Medicine, Niigata, Japan.

METHOD DETAILS

High-throughput Chemical Screening

Delipidation

To comprehensively assess the ability of chemicals to solubilize lipids in a high-throughput manner, we used a previously reported method (Susaki et al., 2014). In brief, 20 μ l of homogenized mouse brain was mixed with 130 μ l of each 10% (wt/wt) chemical solution in 96-well plates and incubated at 37°C overnight. After gentle shaking, the OD600 of the mixture was measured with a PowerWave XS (Bio-Tek). The lipid solubility score was calculated as follows. First, the OD600 of each chemical solution alone was subtracted from the OD600 of the mixture. The lipid solubility score was then determined by plotting the resulting OD600 on a line created by assigning the OD600 of PBS-suspension as 0.0 and the OD600 of the chemical solution alone as 1.0. Among the non-detergent and salt-free chemicals, those that were colored (OD600 \geq 0.1), of low solubility, or lacked a LogP value (octanol-water partition coefficient) were excluded from the chemical profiling. To examine the relationship between tissue phospholipid or cholesterol content and transparency, adult mouse half brains were weighed and then immersed in various delipidating CUBIC chemicals (Figures 2E and S2D). After 1 day of delipidation at 37°C with gentle shaking, the brains were washed with PBS at room temperature for a half day with gentle shaking. The washed samples were then subjected to phospholipid or cholesterol quantification. To quantify the phospholipid content, the samples were thoroughly crushed, then sonicated in 10% Triton X-100 in PBS to obtain a homogenized suspension. After adjusting for the total weight of each sample, the phospholipid was quantified with LabAssay Phospholipid (Wako Pure Chemical Industries, 296-63801) according to the instruction manual, with OD600. The absolute amount of phospholipid was determined by fitting the OD600 value to a standard curve generated by a serially diluted pure phospholipid standard. The cholesterol content was similarly quantified using LabAssay Cholesterol (Wako Pure Chemical Industries, 296-65801).

To measure the relative transparency, delipidated samples were washed with PBS, and immersed in modified ScaleCUBIC-2 [22.5 wt% antipyrine (Tokyo Chemical Industry, D1876), 22.5 wt% sucrose (Nacalai Tesque, 30403-55), 25 wt% urea (Nacalai Tesque, 35904-45), and 10 wt% triethanolamine (Wako Pure Chemical Industries, 145-05605)] overnight at room temperature with gentle shaking. The transmittance was quantified with a Spectral Haze Meter SH 7000 (Nippon Denshoku Industries), as described in our previous study (Tainaka et al., 2014).

After comprehensive screening for effective delipidation chemicals, we further assessed their delipidation ability when used in combination with other chemicals, as shown in Figures 4A–4D, S3A and S3H. Adult mouse half brains, adult mouse kidneys, and human brain blocks were used to evaluate the chemicals' delipidation ability. Each tissue was weighed prior to the experiment if required for normalization. The mouse tissues were immersed in the cocktails for more than 1 day at 37°C with gentle shaking, while the human tissues were immersed in the cocktail for more than 4 days at 37°C with gentle shaking. After delipidation, the samples were washed with PBS overnight. If required to improve the transparency of the tissue, the samples were then subjected to RI-matching procedures, consisting of 1:1-diluted CUBIC-R for one day followed by CUBIC-R for one more day. The washed samples were then subjected to phospholipid quantification as described above.

Decoloring Ability

To comprehensively evaluate the decoloring ability of chemicals in a high-throughput manner, we used a previously reported method (Tainaka et al., 2014) with minor modifications. Because a large amount of blood was required for this screen, we used horse blood (Kohjin-Bio, 12070110). Prior to screening, the blood was fixed in an equal volume of 8% PFA in PBS, and the mixture was then diluted 4-fold with PBS. The fixation was performed at 37°C for 16 hours. After removing clots by filtration, the sample was centrifuged at 1500 G for 3 minutes, and the supernatant was discarded. The pellet was washed with PBS. This centrifugation-washing procedure was repeated for a total of three times. The final pellet was diluted in the same amount of PBS as the original volume of blood. For the comprehensive screening, 50 μ l of fixed blood and 150 μ l of 10% (wt/wt) CUBIC chemical solution were mixed in 96-well plates. The samples were gently shaken for 1 day at 37°C, then spun at 1500 G for 5 minutes, and 100 μ l of the supernatant was transferred to another 96-well plate. OD420 and OD700 were measured with an EnSpire plate reader (Perkin Elmer, USA). To calculate the decoloring score, we first subtracted the OD700 from the OD420 to account for light scattering. The resulting value was then divided by the value obtained for Quadrol. Among the non-detergent and salt-free chemicals, low-solubility chemicals were excluded from the chemical profiling. After this comprehensive screening for decoloring chemicals, we used adult mouse

spleen to examine the chemicals' decolorization ability in biological tissues. An adult mouse spleen was immersed in 3 mL of the CUBIC chemical solutions at 37°C for 3 hours. Then, 100 μ l of each supernatant was subjected to OD400 measurement. These results are summarized in [Figure 2H](#).

RI Matching

To screen for chemicals with effective RI matching, we assumed that such chemicals would satisfy at least two conditions: colorless with a high RI in 10%(wt/wt) solution, and highly soluble in water. To first identify chemicals with a high RI in 10%(wt/wt) solution, we measured the OD400 with a PowerWave XS and the RI value of each CUBIC-chemical solution with an Abbe refractometer (Atago, DR-A1, Japan) ([Figures 3A and 3B](#)). Next, we examined whether the chosen chemicals were soluble in water at 60-70 wt%. The candidates satisfying these two criteria were then evaluated for their clearing performance in mouse lung. Prior to the RI-matching step, the lungs were delipidated with ScaleCUBIC-1 for 2 weeks at 37°C. For [Figures 3C and 3E](#), the lungs were dissected into small (3-5-mm) blocks, which were then immersed into 400 μ l of 60-70 wt% CUBIC chemical at room temperature overnight. The resulting samples were transferred into 96-well plates, and the OD600 was measured with a PowerWave XS. For combinatorial screening, the whole lungs were first immersed in 2 mL of the chemical cocktail diluted 1:1 with deionized water, then gently shaken at room temperature overnight. The lungs were then immersed in 2 mL of the chemical cocktail with gentle shaking at room temperature overnight. Pictures of the samples taken after RI matching are shown in [Figures 4E and S3F](#).

Decalcification

To measure the decalcifying ability of a chemical, we used a screen based on hydroxyapatite (HAp), a major component of bone, as a surrogate for bone. Because the specific gravity of HAp (about 3.16) is much higher than that of water (= 1), we dissolved 200 mg/ml or 100 mg/ml HAp in 40%(v/v) glycerol to prevent its precipitation during the experiments. We then mixed 20 μ l of homogenized HAp solution with 130 μ l of the 10%(wt/wt) chemical solutions in 96-well plates. After gentle shaking at 37°C overnight, the plates were centrifuged at 1500 G for 3 minutes, and the OD600 of the mixture was then measured with a PowerWave XS. The decalcification score was calculated by plotting the resulting OD600 on a line in which the OD600 of PBS-HAp suspension was 0.0 and the OD600 of EDTA-2Na-treated suspension ([Figures 3F and 3I](#)) or EDTA titrated with CU#0414-treated suspension ([Figures 3H and S2M](#)) was 1.0.

Quenching of Fluorescent Proteins (FPs) by Chemicals

The pattern and expression level of FPs in tissue varies due to individual differences, making it difficult to accurately quantify the FP quenching of chemicals, while an *in vitro* FP quenching assay is more quantitative and has higher reproducibility. Moreover, clearing protocols usually involve some kind of chemical fixation (e.g., PFA, glutaraldehyde, or a Clarity-related embedding hydrogel), and the FP signals can be dramatically affected by the fixation conditions (e.g., the fixative chemicals, concentration, duration, and temperature). For these reasons, we conducted an *in vitro* FP quenching assay in this study.

To comprehensively measure the effect of CUBIC chemicals on the fluorescence intensity of fluorescent proteins (FPs), we used EGFP and Sirius ([Figures S1D and S1E](#)). Recombinant EGFP at 0.05 mg/ml and Sirius at 0.2 mg/ml were prepared in PBS. Then, 20 μ l of the FP solutions were mixed with 130 μ l of each 10%(wt/wt) chemical solutions in 96-well plates. After gentle shaking at 37°C overnight, we measured the 507-nm emission for EGFP by 488-nm excitation, and the 427-nm emission for Sirius by 355-nm excitation, with an EnSpire. A series of standard buffers with a pH range of 2-14 was prepared, including 200 mM glycine (pH 2.5, 3, 3.5, 12, 12.5, and 13; Nacalai Tesque, 17109-35), 100 mM citrate (pH 4, 4.5, 5, 5.5, 6, 6.5, and 7; sodium citrate tribasic dehydrate, Sigma-Aldrich, S4641), PBS (pH 7.5 and 8), 10 mM borate (pH 8.5, 9, 9.5, and 10; borate reference solution, Horiba), 50 mM NaHCO₃ (pH 10.5 and 11; Nacalai Tesque, 31212-25), and 100 mM NaH₂PO₄ (pH 11.5; Nacalai Tesque, 31718-15). To further demonstrate the quenching effect of each CUBIC protocol, we also used 16 mg/ml YFP and 15 mg/ml mCherry. The fluorescence intensities of these FPs were measured as described above, using the appropriate excitation and emission wavelengths ([Figures 4F and S3E](#)).

pH evaluation

Because pH can significantly influence the chemical parameters in tissue clearing, we established a high-throughput pH measurement assay using universal pH indicator paper (As One Corp., 1-1254-01). The papers were cut into circles and placed in the bottom of 96-well plates, followed by the application of 2 μ l of CUBIC chemicals. The absorbance at 550, 570, 610, and 660 nm was measured with an EnSpire, then the pH was predicted according to a regression model.

To establish the regression model, we prepared a series of standard solutions with a pH range of 0-14: 200 mM KCl (pH 1, 1.5, and 2; Nacalai Tesque, 28514-75), 200 mM glycine (pH 2.5, 3, 3.5, 12, 12.5, and 13; Nacalai Tesque, 17109-35), 100 mM citrate (pH 4, 4.5, 5, 5.5, 6, 6.5, and 7; sodium citrate tribasic dehydrate, Sigma-Aldrich, S4641), PBS (pH 7.5 and 8), 10 mM borate (pH 8.5, 9, 9.5, and 10; borate reference solution, Horiba), 50 mM NaHCO₃ (pH 10.5 and 11; Nacalai Tesque, 31212-25), and 100 mM NaH₂PO₄ (pH 11.5; Nacalai Tesque, 31718-15). The pH of the standard solutions was adjusted with hydrochloric acid or sodium hydroxide, and measured with a benchtop pH meter (Horiba, LAQUA F-71). The predicted pH values were less accurate in the low (pH < 3) or high (pH > 12) pH range by the single linear regression model. Therefore, we introduced three regression models: an acid-range, a neutral-range, and a base-range regression model. The pH was first predicted with the neutral-range regression model. If the predicted pH was higher than 11.1, then the base-range regression model was applied. If the predicted pH was lower than 5.5, then the acid-range regression model was applied. These thresholds were statistically determined by comparing the mean square error of the predicted pH and the measured pH.

Concern about Potential False Negatives

Each chemical was used as a 10%(wt/wt) solution in all of the first chemical screenings. We hoped to minimize false negatives in the first screening, so we would not miss potential candidates. Although chemicals were likely to have concentration-dependent effects on each parameter, we could avoid false negatives by taking advantage of the chemical diversity of our chemical library. That is, owing to our comprehensive chemical profiling, we could predict whether the performance of a chemical in the first screening was under-estimated or not from its chemical structure.

We also considered the possibility of chemicals with more dramatic concentration-dependent behavior. Concentration-dependent self-aggregation of the solute is one of the most likely causes of dramatic concentration-dependent behavior. In aqueous medium, hydrophobic chemicals precipitate and amphiphilic chemicals form micelles in a concentration-dependent manner. Since precipitates would have no effect on tissue clearing, we focused on the ability of amphiphilic chemicals such as detergents to form water-soluble micelles. To avoid false negatives in the amphiphilic chemicals, we prepared a wide variety of detergents, as shown in Figure S2B. In this figure, we categorized a series of detergents according to the polarity head group, because each group of detergents forms micelles with similar chemical properties at concentrations above the critical micelle concentration (CMC). In general, the CMC of a detergent tends to decrease as the hydrophobic part of the detergent molecule grows. Figure S2B indicates that the micelle state exhibited much higher delipidation activity than the monomer state. This means that amphiphilic chemicals with a high CMC were potential false negatives in our delipidation screening. That is, the delipidation efficiency of these chemicals *in vitro* may be much higher at concentrations above the CMC. However, micelle molecules are liable to have low permeability in real tissue as described above, and higher solute concentrations often have a quenching effect on fluorescent proteins. Thus, we did not perform additional experiments on the concentration dependence of such amphiphilic chemicals. In the decoloring screen, micelle molecules had a similar tendency for low permeability as in real tissue (Figure 2H). For the RI matching and decalcification assays, we did not observe significant positive outputs for amphiphilic chemicals.

Taken together, our chemical profiling approach applies chemical insights and hypotheses to tissue clearing, and these insights are helpful for preventing potential false-negatives. Of course, our profiling is not perfect for false-negative detection due to unknown chemical phenomena. Nevertheless, we are confident that our screening system has sufficient detection sensitivity without redundancy and complexity to be useful for this field at the present time.

Comparison of Organic Solvents and Hydrophilic Chemicals

To examine the effects of organic solvents and hydrophilic chemicals, we included several organic solvents in this study, such as tetrahydrofuran (THF, CU#1427), dimethyl sulfoxide (DMSO, CU#1510), 2-propanol (CU#1514), methanol (CU#1515), ethanol (CU#1516), benzyl alcohol (CU#1517), benzyl benzoate (CU#1518), acetone (CU#1520), 1,4-dioxane (CU#1521), acetonitrile (CU#1522), ethyl acetate (CU#1523), and *N,N*-dimethylformamide (DMF, CU#1524). However, we could not perform a comprehensive evaluation of organic solvents due to experimental feasibility. First, almost all organic solvents (e.g., dichloromethane and diphenyl ether), with the exception of several alcohols and aprotic polar solvents, as listed, are immiscible with water. Second, plastic experimental tools (e.g., microtubes and microplates) are highly labile to many organic solvents (especially at high concentration). Therefore, we included only the above-listed organic solvents in this study. In our chemical screening, we prepared 10%(wt/wt) aqueous mixtures of the organic solvents because of the above concerns and to make fair comparisons. However, these aqueous mixtures displayed quite low performances (see Table S2); thus, organic solvents would exert their clearing performance at a high concentration or in a fully dehydrated condition.

Chemical Parameters

To obtain a chemical profile for the chemicals identified from the screens, we analyzed a series of chemical parameters (e.g., LogP and PSA) using the ChemOffice software. The LogP and LogS value of each chemical was calculated by the MOSES descriptor Community edition (<https://www.mn-am.com/services/mosesdescriptors>). Solubility parameters (e.g., dD and dP) of each chemical were calculated based on the Hansen solubility parameters (Hansen, 2007). The stability constant of various chemicals for Ca²⁺ ion according to the NIST Standard Reference Database 46 was used (Smith et al., 2003).

Multivariate Linear Regression Analysis

We prepared a series of parameters consisting of three classes of parameters: functional parameters, solubility parameters (calculated by Hansen solubility parameters), and structural and topological parameters (Figure S1F). The lists of parameters used for delipidation, decolorization, and RI matching are shown in Figure 2C, S2I, and 3D, respectively. After normalizing the scores and parameters, we performed partial least-squares (PLS) regression using four major PLS components. The variable importance in projection (VIP) scores of two major PLS components were calculated from the results.

CUBIC Protocols

CUBIC Protocol I for Adult Mouse Organ Samples and Marmoset Brain

For the efficient clearing of mouse organs, we first performed an optional transcatheter perfusion of CUBIC-P reagents. After the mouse was sacrificed by an overdose of pentobarbital, 15 mL of PBS was perfused followed by 20 mL of 4% PFA-PBS. After another 15 mL of PBS was perfused, the transcatheter perfusion of 100 mL of CUBIC-P [mixture of 5 wt% 1-methylimidazole (Tokyo Chemical Industry, M0508), 10 wt% CU#0414 (*N*-Butyldiethanolamine, Tokyo Chemical Industry, B0725) and 5 wt% Triton X-100

(Nacalai Tesque, 12967-45)] from the left ventricle for 10 minutes was performed. After perfusion, the organs were dissected and directly immersed in CUBIC-L (mixture of 10 wt% CU#0414 and 10 wt% Triton X-100). The organs in CUBIC-L were incubated with shaking at 37°C for 3-7 days. The immersion period was based on the sample size. If the immersion period was longer than 4 days, the CUBIC-L was refreshed at least once. After delipidation, the organs were washed in PBS with gentle shaking at room temperature overnight. If required, the organs were stained with RedDot 2 (1:100, Biotium Inc, #40061) or propidium iodide (10 µg/ml, PI; Life Technologies, P21493) in 0.1 M phosphate buffer (PB) containing 0.5 M NaCl with shaking at room temperature for 3-5 days. The organs were then immersed in 1:1 water-diluted CUBIC-RA [recommended for FP-expressing organs, a mixture of 45 wt% CU#0640 (antipyrine, Tokyo Chemical Industry, D1876) and 30 wt% CU#1283 (*N*-methylnicotinamide, Tokyo Chemical Industry, M0374)] or in 1:1 water-diluted CUBIC-R [for other organs, mixture of 45 wt% CU#0640 and 30 wt% CU#0855 (nicotinamide, Tokyo Chemical Industry, N0078)] with gentle shaking at room temperature for 1 day. The organs were then immersed in CUBIC-RA or CUBIC-R with gentle shaking at room temperature for 1-2 days. The pH of CUBIC-R and CUBIC-RA can be optionally adjusted to approximately 8-9 with CU#0414. If required, the cleared organs were embedded in CUBIC-agarose gel [2% agarose (Nacalai Tesque, 01163-76) dissolved in CUBIC-RA or CUBIC-R].

The clearing and staining of adult marmoset brain was performed as follows. The marmoset was sacrificed by an overdose of pentobarbital (> 100 mg/kg, Nacalai Tesque, 02095-04), then transcardially perfused with 200 mL of cold PBS (pH 7.4) and 300 mL of 4% PFA-PBS. The brain was dissected, then post-fixed with 4% PFA-PBS at 4°C overnight. After washing in PBS, the brain was immersed in CUBIC-L with shaking at 37°C for a total of 5 weeks, and then at 45°C for 1 week. The CUBIC-L was refreshed every 1-2 days throughout the delipidation. After washing in PBS, the brain was immersed in 10 µg/ml propidium iodide (PI) in PB containing 1.5 M NaCl with shaking at 37°C for a total of 19 days. The staining solution was refreshed after day 12. After washing in PBS, the brain was immersed in 10 wt% imidazole (Tokyo Chemical Industry, I0001) aqueous solution with gentle shaking at room temperature for 3 days. The imidazole solution was refreshed every day. The brain was then immersed in 1:1 water-diluted CUBIC-R (pH adjusted to approximately 8-9 with CU#0414) with gentle shaking at room temperature for 3-4 days. Finally, the brain was immersed in CUBIC-R (pH adjusted to approximately 8-9 with CU#0414) with gentle shaking at room temperature for 7 days. The CUBIC-R was refreshed after day 4.

CUBIC Protocol II for Mouse Body or Tissues That Include Bone

PFA-fixed samples were immersed in CUBIC-L with shaking at 37°C for 3-7 days, then washed with PBS at room temperature overnight. The immersion period was based on the sample size. If the immersion period was longer than 4 days, the CUBIC-L was refreshed at least once. The samples were immersed in CUBIC-B [10 wt% EDTA (Nacalai Tesque, 15105-35) and 15 wt% imidazole] with shaking at 37°C for 5-7 days, then washed with PBS at room temperature overnight. During decalcification, the CUBIC-B was refreshed at least once. The samples were immersed in CUBIC-L with shaking at 37°C for 2-4 days, then washed with PBS at room temperature overnight. If required, the organs were stained with 10 µg/ml PI in 0.1 M PB containing 0.5 M NaCl with shaking at 37°C for 5-7 days. The samples were immersed in 1:1 diluted CUBIC-RA or CUBIC-R with gentle shaking at room temperature for 1 day. The samples were then immersed in CUBIC-RA or CUBIC-R with gentle shaking at room temperature for 1-2 days. If required, the cleared samples were embedded in CUBIC-agarose gel.

CUBIC Protocol III for Aggressive Tissue Clearing

Human tissues were stored in formalin at 4°C until use. The dissected blocks were washed with PBS overnight prior to clearing. The tissue blocks were immersed in CUBIC-HL [mixture of 10 wt% CU#0070 (1,3-bis(aminomethyl)cyclohexane, Tokyo Chemical Industry, B1005) and 10 wt% CU#0631 (sodium dodecylbenzenesulfonate, Tokyo Chemical Industry, D0990), whose pH was adjusted to 12.0 by *p*-toluenesulfonic acid (Tokyo Chemical Industry, T0267)] with shaking at 37°C (for human brain or kidney) or 45°C (for human heart, liver, lung, or spleen) for 1-2 weeks, then washed with PBS at room temperature. The immersion period was based on the sample size. Since the apparent opacity inside the sample gradually disappears as delipidation progresses, the delipidation period could be easily judged by the appearance of the sample soaked in CUBIC-HL. Note that prolonged delipidation may damage the sample morphology. If delipidation needs to be prolonged beyond 2 weeks, we recommend that the subsequent delipidation be done at a lower temperature or in CUBIC-L. During delipidation, the CUBIC-HL should be refreshed at least once. If required, the organs were stained with 10 µg/ml PI in 0.1 M PB containing 0.5 M NaCl with shaking at 37°C for 5-7 days. After washing in PBS, the samples were immersed in 1:1 diluted CUBIC-R with gentle shaking at room temperature for 1 day. The samples were then immersed in CUBIC-R with gentle shaking at room temperature for 1-2 days. If required, the cleared organs were embedded in CUBIC-agarose gel.

CUBIC Protocol IV for Large Blocks of Human Brain Tissue

Human brain blocks were stored in phosphate-buffered formalin at 4°C until use. The dissected blocks (around 1 cm³) were washed with PBS overnight prior to clearing. The brain blocks were immersed in CUBIC-L with shaking at 45°C for 1-2 weeks, then washed with PBS at room temperature. The immersion period was based on the volume of white matter. During delipidation, the CUBIC-L was refreshed at least once. After washing in PBS, the samples were immersed in 1:1 diluted CUBIC-R with gentle shaking at room temperature for 1 day. The samples were then immersed in CUBIC-R with gentle shaking at room temperature for 1-2 days. We noted that the autofluorescence of cerebral cells decreased as the delipidation period increased. We recommend that delipidation be finished by approximately one week to preserve sufficient autofluorescent signals. If required, the cleared samples were embedded in CUBIC-agarose gel.

Deformation Analysis of Cleared Brains

Brains after PBS, CUBIC protocol I without pH adjustment, and CUBIC protocol I with pH adjustment to 8–9 were subjected to deformation analysis. Two brains were prepared for each procedure, and then projection images were captured by a ChemiDoc XRS Plus (Bio-Rad). The brains were manually segmented, then registered to a standard post-fixed brain. The average of the two obtained deformation fields was visualized and mapped onto a representative projection image of the brain.

Long-term Tissue Preservation

To preserve the cleared tissue for a long time, we recommend storing it in O.C.T. compound at -80°C after washing it with PBS as described in our previous paper (Susaki et al., 2015). In this storage medium, FP signals can be preserved for several months to years.

Immunostaining

For Figure 5D, an 8-week-old ICR mouse brain was washed with PBS after 4 days of delipidation with CUBIC-HL. The brain was immersed in 40% sucrose for 1 day, embedded in O.C.T. compound (Sakura Finetek), and sectioned with a cryostat (CM3050S, Leica). The brain sections were immersed in 200 μl of PBST with 1% anti-GFAP-Cy3 (C9205, Sigma-Aldrich) or 0.1% anti-NeuN (MAB377, Millipore) antibodies. For NeuN detection, a secondary antibody (A21203, Thermo Fisher Scientific) was applied. For Figure 5F, the human brain was washed with PBS overnight and sliced after 9 days of delipidation with CUBIC-L (CUBIC protocol IV). The slice was placed into 400 μl of immunostaining buffer (mixture of PBS, 0.5% Triton X-100, 0.25% casein, and 0.01% NaN_3) containing 1:20 diluted rhodamine-conjugated lectin (RL-1062, Vector Laboratories) or 1:10 diluted Alexa647-conjugated α -SMA (alpha smooth muscle actin) antibody (IC1420R, Novus Biologicals) for 5 days at room temperature with gentle shaking. For the control experiment, the immunostaining buffer without antibody was applied. After washing the samples with PBS for several hours, the samples were immersed into CUBIC-R according to CUBIC protocol IV.

Microscopy

Light-sheet Fluorescence Microscopy (LSFM)

Macroscopic whole-body or organ images were acquired with two custom-built LSF microscopes (MVX10-LS, developed by Olympus). Images were captured using a 0.63 \times objective lens [numerical aperture (NA) = 0.15, working distance = 87 mm] with digital zoom from 1 \times to 6.3 \times . The first LSF microscope was equipped with lasers emitting at 488 nm, 532 nm, 590 nm, and 639 nm. The second was equipped with lasers emitting at 488 nm, 532 nm, 594 nm, and 637 nm. When the stage was moved to the axial direction, the detection objective lens was synchronically moved to the axial direction to avoid defocusing. The RI-matched sample was immersed in an oil mixture (RI = 1.525) composed of silicon oil HIVAC-F4 (RI = 1.555, Shin-Etsu Chemical) and mineral oil (RI = 1.467, M8410, Sigma-Aldrich) during image acquisition.

A customized light-sheet microscope was used for the high-resolution-imaging of the organs of adult mice in Figure S5. Fluorescence excited by a 488 nm CW laser (Omicron, SOLE-3) was captured with a sCMOS sensor (Andor, Neo) using a 10 \times objective lens (XLPLN10XSVMP, NA = 0.6, working distance = 8 mm, Olympus). The details of the light-sheet microscope are described in our previous study (Murakami et al., 2018). To obtain complete views, the regions of interest were divided into 7 \times 4 tiles (for the left medial lobe of the mouse liver), or 6 \times 8 tiles (for the left lung of the mouse). Images were collected by scanning the sample in the z-direction, with a step size of 5 μm .

Confocal Microscopy

An upright confocal microscope (FV1200, Olympus) was used for microscopic 3D imaging. The microscope was equipped with a 25 \times objective lens (XLSLPLN25XGMP, NA = 1.0, WD = 8.0 mm, Olympus). A 473 nm laser was used for image acquisition. During image acquisition, RI-matched samples were immersed in a mixture of silicon oil (RI = 1.525) as described above.

In Vivo Bioluminescence Imaging

Mice were anesthetized with avertin, and D-luciferin potassium salt (Promega) was injected intraperitoneally. Ten to fifteen minutes after injection, the luciferase activity was measured using a NightOWL II LB983 (Berthold Technologies GmbH & Co. KG, Bad Wildbad, Germany).

Histological Examination

After CUBIC-based clearing, biological samples were washed with PBS, embedded in paraffin, and subjected to HE staining as previously described (Hoshino et al., 2015) and to a series of immunostainings (Figures 5E and S6I).

Image Analysis

The Analysis of Cellular Nuclei

The cellular nuclei in organs were comprehensively detected by our image-processing pipeline (Murakami et al., 2018). The process can be divided into two steps: 2D detection of cells and 3D unification of multiply detected cells. The 2D detection of cells was performed by detecting local maxima after applying a mean filter to raw images. Then, 3D local maxima were detected after a 3D mean filter was applied to the 2D-detected cells. The detected cellular nuclei (“points” or “point clouds”) were further analyzed for the segmentation of tubular structures. To this end, we used the alpha shape function with the specific alpha radius by using MATLAB. The

alpha radius was set at 30 μm for liver and 50 μm for lung. After forming the alpha shape, the surface points composing the alpha shape were used. Since the surface points also included cells located in the outer layer of the organ, we removed those points by applying a manually generated mask. The points are shown in red or magenta in [Figures S5J](#) and [S5L](#).

Multi-directional Image Fusion

For [Figures 6](#), [7](#), [S5](#) and [S6](#), multi-directional image fusion was performed after the acquisition of images from multiple directions unless noted. All the samples were embedded in agarose, and mounted in the LSF microscope. We first performed the imaging with both optical arms of the LSF microscope (i.e., left and right) from one direction (top-to-bottom). The samples were then flipped 180° manually, followed by image acquisition (bottom-to-top) with both optical arms. The imaging sequences were then repeated for multi-color imaging. These processes produced four stacks per channel: a right-side-illuminated top-bottom stack (TB-R), left-side-illuminated top-bottom stack (TB-L), right-side-illuminated bottom-top stack (BT-R), and left-side-illuminated bottom-top stack (BT-L). For the registration process, we set the TB-L stack as the fixed images, then three other stacks were registered to TB-L stack. Prior to registration, the stacks were reduced to less than 4 GB by cropping marginal regions, or by downsampling them into isotropic voxel sizes to reduce the computational cost. Then, TB-R and BT-L were directly registered onto TB-L with an affine transformation using ANTs ([Avants et al., 2011](#)). Because the direct registration of BT-R to TB-L often ends in misalignment due to the intensity gaps of these two stacks, we performed indirect registration by registering BT-R onto BT-L, followed by the application of the affine matrix obtained from the registration of BT-L onto TB-L. These mutually registered images were fused using the Fiji software, Multiview Reconstruction ([Schindelin et al., 2012](#)).

Segmentation

For segmentation of the mouse kidney glomeruli in [Figure S5](#), we used HLoG (Hessian based Difference of Gaussian) developed by Zhang et al. ([Zhang et al., 2015](#)) with minor modifications. In the original paper, renal glomeruli were extracted by unsupervised clustering. Because this method was originally optimized for MRI-scanned images and therefore could not show high accuracy, we introduced a manual threshold for the smallest eigenvalue to achieve higher accuracy.

For the segmentations of metastatic cancer in [Figures 6H](#) and [7H](#), the thresholds were applied based on absolute intensity. Manual segmentation was performed to segment the human kidney glomeruli ([Figures 6J](#) and [6K](#)).

Virtual Multiplex Fluorescence Imaging and Analysis of Whole Brain

Fluorescently labeled mouse brains were stained with a far-red nuclear stain, RedDot 2, prior to the RI-matching process. The cleared brains were embedded in agarose gel as mentioned above. Brain images were captured using a 0.63 \times objective lens with a 1.25 \times zoom. The brain structures were visualized by the RedDot 2 fluorescent signal at 637-nm excitation. The sectional images were taken at 7.5- μm steps from both the right and left sides with a fixed focal position of the light sheet. The FP signal was then visualized using a laser of appropriate wavelength with sequential shifting of the focal position of the light sheet. The thinnest focal point of the LSF microscope was horizontally scanned 6 times per plane to reduce defocus derived from the Gaussian shape of the beam. The scanning with focus shifts was performed from both sides of the illumination arm as described previously ([Gao, 2015](#); [Santi et al., 2009](#)).

The images of the identical horizontal positions (2 images for RedDot 2 signal, or 12 images for FP signals) were fused using the content-based fusion algorithm proposed by Preibisch et al. ([Preibisch et al., 2009](#)). To register individual brains, the fused volumetric nucleus images were downsampled 5:1 in one direction. These downsampled images were registered using the ANTs software in the symmetric normalization (SyN) manner. The obtained transformation information was applied to the original volumetric FP images, thus achieving registration without losing the resolution. To apply the transformation information to large data, we used our customized MATLAB code, because direct application of the transformation with the default algorithm in ANTs requires a huge amount of memory, which makes it practically impossible. The overall process (fusion, registration, application of transformation information) was fully automated.

Volume Rendering and Image Visualization

To generate the tubular structures shown in [Figures S5K](#) and [S5M](#), visual mapping of the alpha shape was implemented by MATLAB. For other volume rendered images, Imaris software (version 8.1.2, Bitplane) was used. The section images were generated by Imaris or Fiji software.

QUANTIFICATION AND STATISTICAL ANALYSIS

Protein Quantification

Human brain tissue was weighed and then immersed in PBS, ScaleCUBIC-1, CUBIC-L, or CUBIC-HL. After 4 days of delipidation at 45°C with gentle shaking, the brain samples were washed with PBS at room temperature for half a day with gentle shaking. The washed samples were then subjected to protein quantification. To quantify the residual protein content, the samples were thoroughly crushed, then sonicated in 1% Triton X-100 in PBS to obtain a homogenized suspension. After adjusting for the total weight of each sample, the protein was quantified with the Microplate BCA Protein Assay Kit-Reducing Agent Compatible (ThermoScientific, #23252) according to the instruction manual, with OD570. The absolute amount of protein was determined by fitting the OD570 value to a standard curve generated by a serially diluted pure Albumin standard.

Quantification of Image Quality

We used discrete cosine transformation Shannon entropy (DCTS) (Royer et al., 2016) to quantify the image quality. The DCTS calculation was performed for every plane image in Figure S5B, and for every 10 plane images in Figures S5H and S5I.

Statistical Analysis

Statistical analyses were performed by R version 3.1.0. and Origin 2016 (OriginLab, Northampton, MA, USA).

For the chemical profiling involving functional analysis and pH dependency (Figures 2A, 2B, 2G, 3A, 3F, S1E, and S2H), normality was evaluated by the Kolmogorov-Smirnov test with a significance level of 0.05. These analyses showed that not all members of the group were normal. The chemical functional group and pH dependency were compared to the control (alcohol group and pH 7-8, respectively) by the Steel test.

For the other chemical analyses, normality was evaluated by the Kolmogorov-Smirnov test with a significance level of 0.05. When all of the members of the group were normal, the homogeneous variance for each group was evaluated by Bartlett's test with a significance level of 0.05. When all of the groups were normal distributions with equal variance, the Turkey-Kramer test was used, when the groups were normal distributions without equal variance, the Games-Howell test was used, and otherwise the Steel-Dwass test was applied. In this study, $p < 0.05$ was considered as significant (* $p < 0.05$, ** $p < 0.01$, *** $p < 0.001$, and n.s. for not significant evaluations).

DATA AND SOFTWARE AVAILABILITY

Our customized MATLAB codes used for the virtual multiplex fluorescence imaging and analysis are publicly available at https://github.com/DSP-sleep/Landscape_pipeline. The other computer codes used in this study are available upon request.

Supplemental Information

Chemical Landscape for Tissue Clearing

Based on Hydrophilic Reagents

Kazuki Tainaka, Tatsuya C. Murakami, Etsuo A. Susaki, Chika Shimizu, Rie Saito, Kei Takahashi, Akiko Hayashi-Takagi, Hiroshi Sekiya, Yasunobu Arima, Satoshi Nojima, Masako Ikemura, Tetsuo Ushiku, Yoshihiro Shimizu, Masaaki Murakami, Kenji F. Tanaka, Masamitsu Iino, Haruo Kasai, Toshikuni Sasaoka, Kazuto Kobayashi, Kohei Miyazono, Eiichi Morii, Tadashi Isa, Masashi Fukayama, Akiyoshi Kakita, and Hiroki R. Ueda

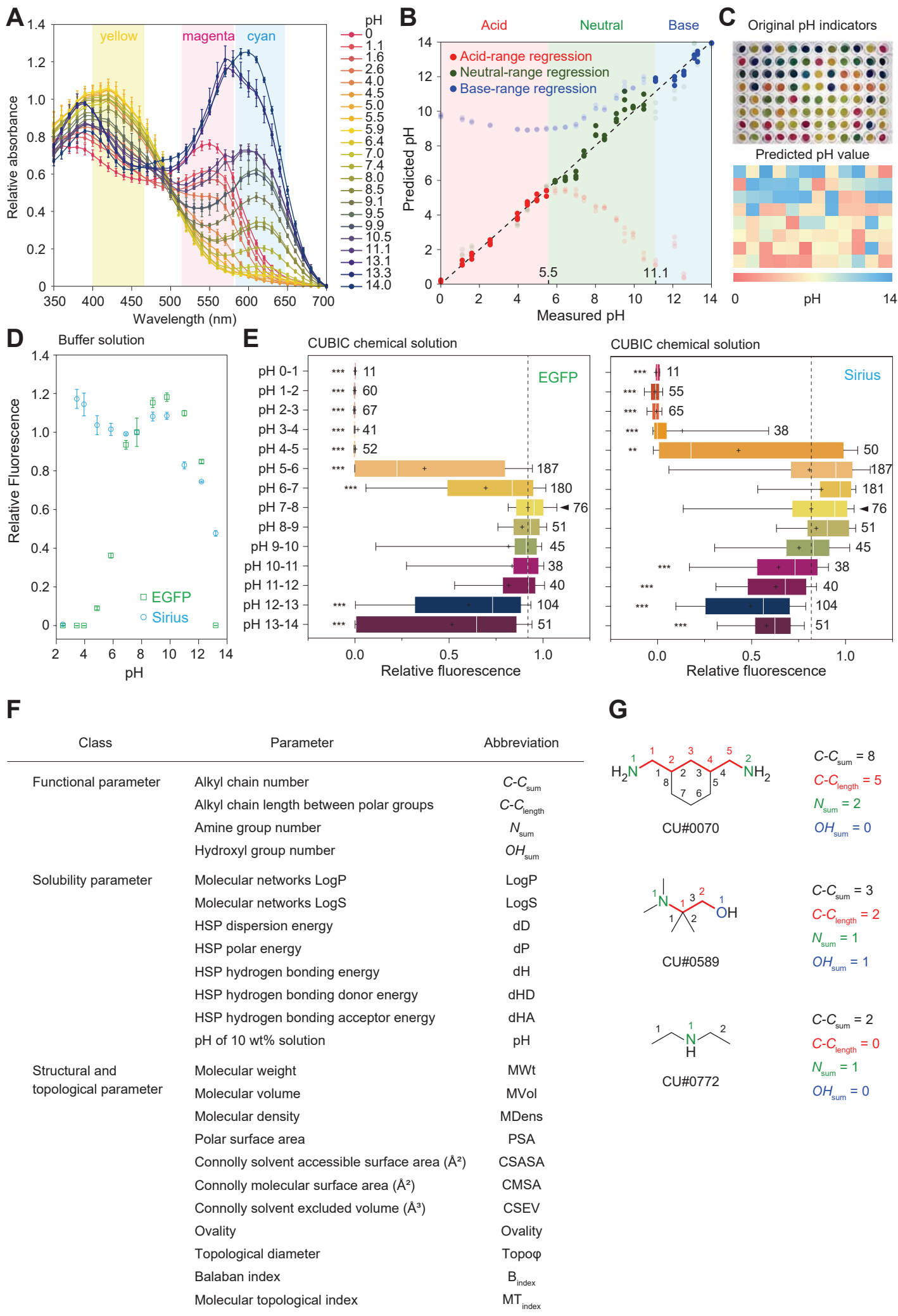


Figure S1

Figure S1. High-throughput pH and Fluorescent Protein (FP) Signal Quenching Estimation Assay, Related to Figures 1-3.

(A) Absorbance spectra of pH indicator papers after their immersion in pH standard solutions. To determine the pH of the chemical solutions, we measured the absorbance at 550, 570, 610, and 660 nm of pH indicators soaked in each chemical solution. Data are mean \pm SD ($n = 3$). (B) Relationship between predicted pH and measured pH with three regression models. The pH of chemicals was first evaluated with the neutral-range regression model, then regressed again with an acid-range or base-range regression model for more accuracy. (C) Image of the pH indicators soaked in CUBIC chemical solutions (top) and predicted pH (bottom). (D) pH dependency of the relative intensity of each FP in buffer solutions. Various pH conditions were examined. Data are mean \pm SD ($n = 2$). (E) Dependency of the relative fluorescence intensity of EGFP (left) and Sirius (right) on the pH of CUBIC chemical solutions compared with pH 7-8. Box and whisker plots show the 25th–75th percentile (boxes), 10th–90th percentile (whiskers), median (vertical lines), and mean (cross). The numbers next to the plots are the numbers of the chemicals. (F) Classes and abbreviations of parameters used in the chemical analysis in this study. (G) Examples of counting functional groups. $**p < 0.01$, and $***p < 0.001$, see also **STAR Methods** for details.

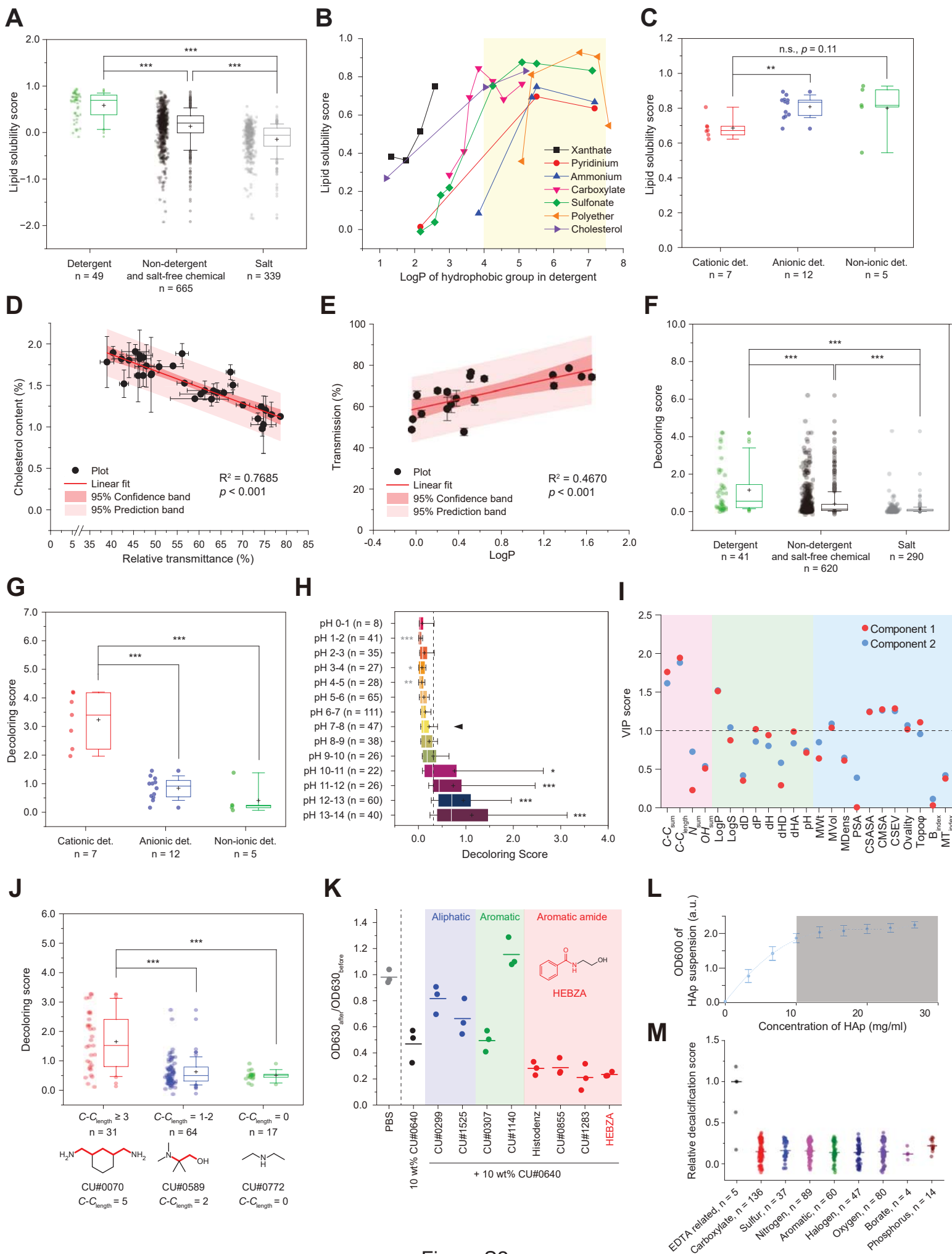


Figure S2

Figure S2. Comprehensive CUBIC Chemical Profiling for Delipidation, Decoloring, RI match, and Decalcification, Related to Figures 2-3.

(A) CUBIC chemicals were divided into three groups (detergents, non-detergent and salt-free chemicals, and salts) and their lipid solubility scores were compared. (B) Relationship between the LogP of the hydrophobic group in a detergent and the lipid solubility score. A series of detergents bearing seven different kinds of polar head group (xyanthate, pyridinium, ammonium, carboxylate, sulfonate, polyether, and cholesterol) was investigated. (C) Lipid solubility scores of cationic, anionic, and non-ionic detergents. Anionic and non-ionic detergents had higher lipid solubility scores than cationic detergents. (D) Scatter plot of the relative transmittance and cholesterol content of brain hemispheres of adult mice treated with high lipid-solubilizing chemicals. Data are mean \pm SD (n = 2). (E) Scatter plot of the relative transmittance and LogP of the amine groups. Data are mean \pm SD (n = 2). (F) CUBIC chemicals were divided into three groups (detergents, non-detergent and salt-free chemicals, and salts) and their decoloring scores were compared. (G) Decoloring scores of cationic, anionic, and non-ionic detergents. Cationic detergents showed better decoloring ability than anionic or non-ionic detergents. (H) Dependency of decoloring scores on pH compared with pH 7-8. (I) VIP scores of two major components for each variance among decoloring amines that had a high delipidation efficiency. (J) The amines were divided into three groups: multipolar amines with $C-C_{\text{length}} \geq 3$, multipolar amines with $C-C_{\text{length}} 1-2$, and single amines ($C-C_{\text{length}} = 0$). Multipolar amines with $C-C_{\text{length}} \geq 3$ exhibited a marked decoloring ability compared to the other amines. (K) The variation in OD630 of human brain samples treated with 10/30 wt% CU#0640/RI candidates were compared. The 8 chemicals were divided into three groups: aliphatic compounds, aromatic compounds, and aromatic amides. "HEBZA" indicates *N*-(2-hydroxyethyl)benzamide. We used 10 wt% CU#0640-based cocktails due to the low water-solubility of HEBZA. (L) Quantitativeness of the HAp-based screening system in **Figure 1E**. OD600 of the HAp suspension increased linearly as the HAp

concentration was raised from 0 to 10 mg/ml. Data are mean \pm SD (n = 4). **(M)** Relative decalcification scores of chemical cocktails containing various kinds of acids listed in the CUBIC chemical library. All of the acids were neutralized with CU#0414 (pH 7-8). Over 200 acids bearing various kinds of functional groups were tested. In this analysis, we compared the tested acids except for EDTA-related chemicals according to their functional group. Box and whisker plots show 25th–75th percentile (boxes), 10th–90th percentile (whiskers), median (horizontal lines), and mean (cross). * $p < 0.05$, ** $p < 0.01$, and *** $p < 0.001$, see also **STAR Methods** for details.

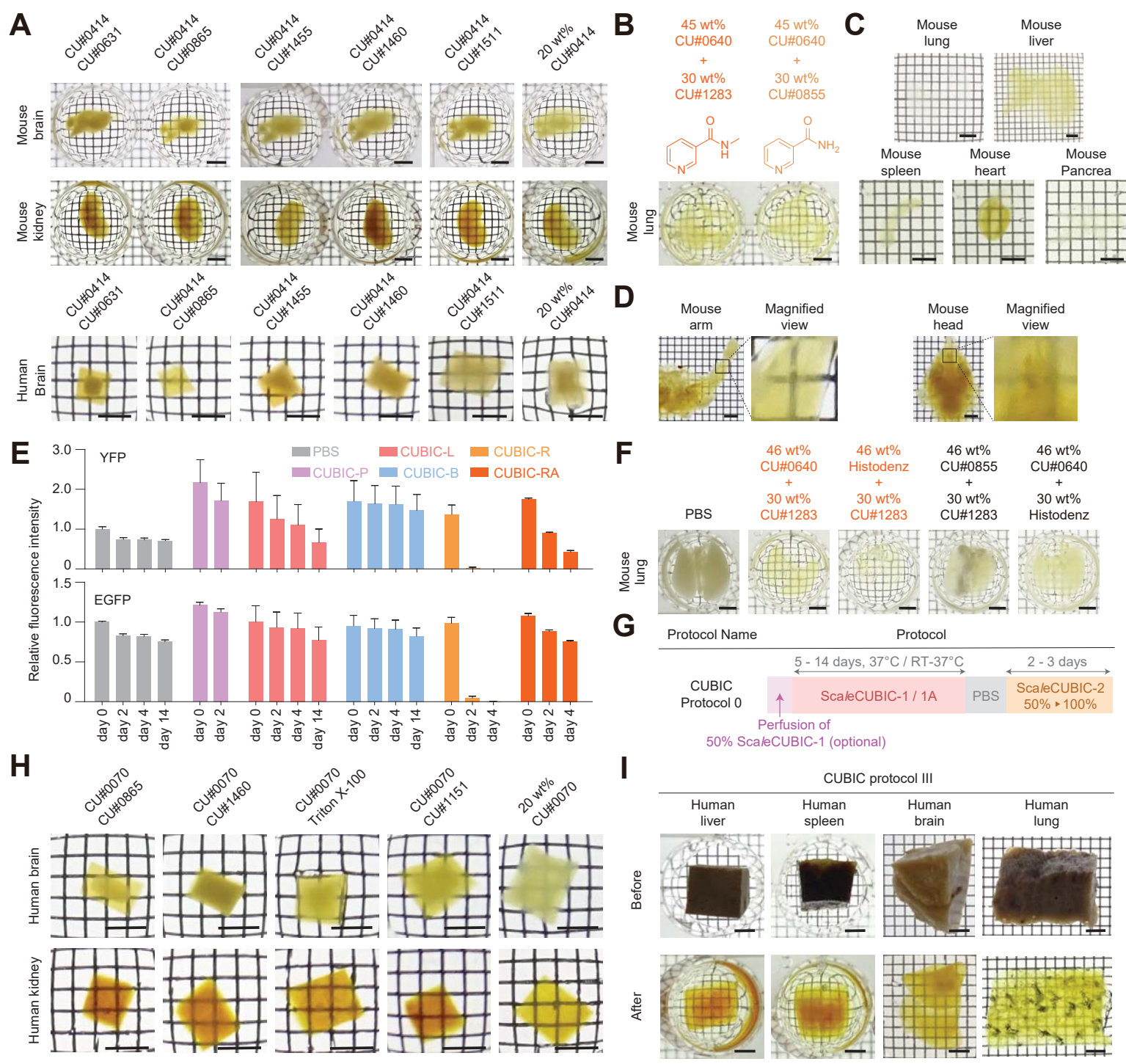


Figure S3

Figure S3. Combinatorial Screening of CUBIC Chemicals for Rapid and Scalable Tissue-Clearing CUBIC Protocols, Related to Figure 4.

(A) Combinatorial screening of delipidation chemicals compatible with FP (related to **Figure 4A**). Mouse brain hemispheres, kidneys, and human brain blocks were delipidated with individual chemical cocktails, and then immersed in CUBIC-R. (B) RI matching performance of the CUBIC-RA cocktail of CU#0640 and CU#1283, and the CUBIC-R cocktail of CU#0640 and CU#0855. Adult (8-week-old) mouse lungs were delipidated and then treated with CUBIC-RA or CUBIC-R. Similar clearing performances were observed. (C) Clearing performance of CUBIC protocol I for various adult (6-week-old) mouse organs. (D) Clearing performance of CUBIC protocol II for adult (8-week-old) mouse arm and head. (E) Time course of fluorescent signals of EGFP and YFP with each CUBIC cocktail. Data are mean \pm SD (n = 3). (F) Combinatorial screening of RI-matching reagents. Delipidated adult (8-week-old) mouse lungs were immersed in the highly concentrated chemical cocktails. (G) Original CUBIC protocol, named as CUBIC protocol 0 hereafter. (H) Combinatorial screening of CU#0070-based delipidation reagents (related to **Figure 4C**). Human tissue blocks were delipidated with individual chemical cocktails, and then immersed in CUBIC-R. (I) Clearing performance of CUBIC protocol III for large blocks of various kinds of human tissues. Scale bars indicate 4 mm.

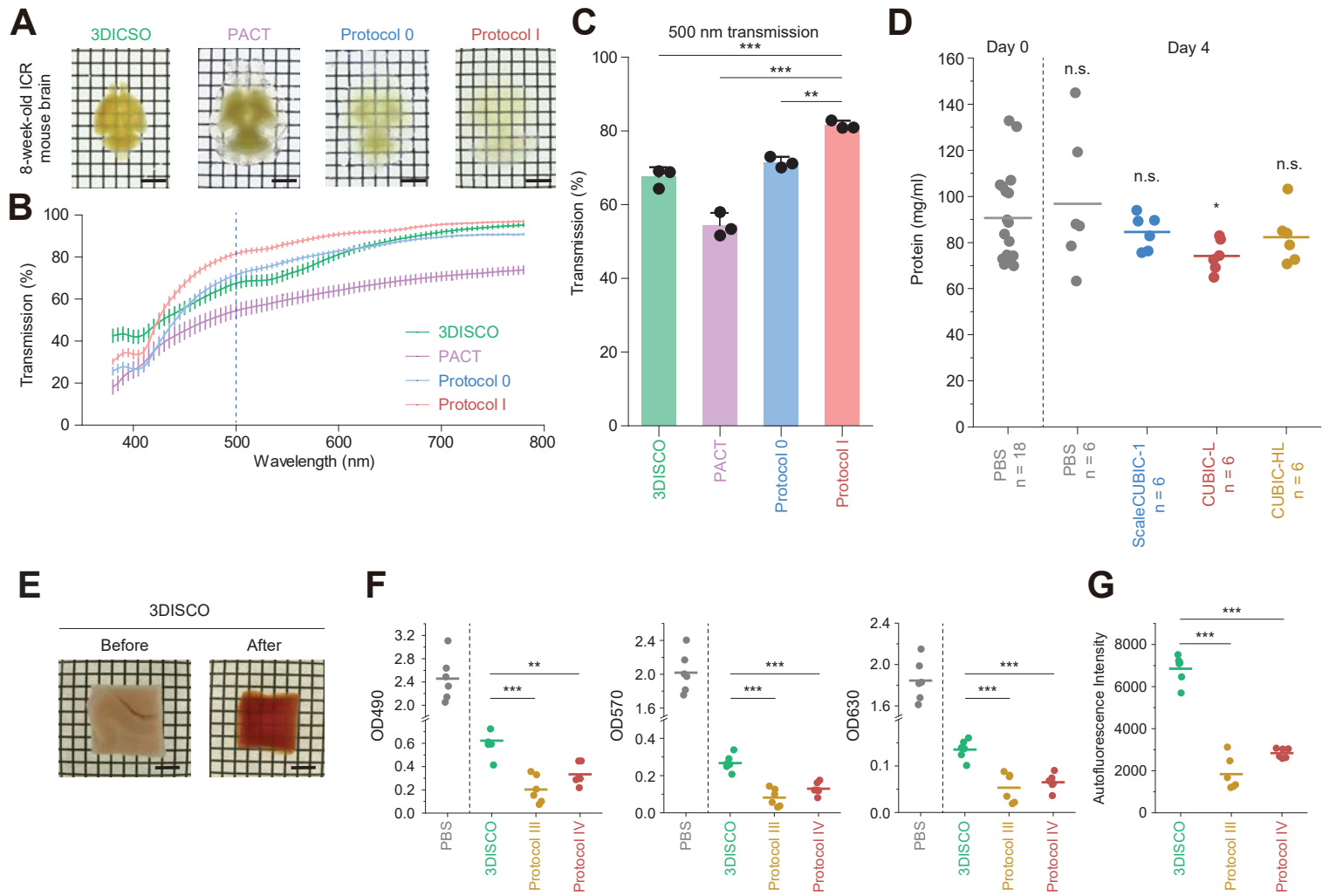


Figure S4

Figure S4. Comparison among Tissue Clearing Protocols, Related to Figure 5.

(A-C) Comparison of clearing protocols. 3DISCO, PACT, CUBIC protocol 0, and CUBIC protocol I were compared. Adult (8-week-old) mice were used. White-background transmission images (A) and quantified transmission (B and C) are shown. Data are mean \pm SD ($n = 3$). Transmission spectrum (B) and transmission of the 500-nm wavelength in B (C) are shown. (D) Quantification of the protein content of human brain tissue after delipidation. Mean are shown. (E) Clearing performance of 3DISCO for human brain block. Scale bars indicate 4 mm. (F) Absorbance at 490 nm, 570 nm, and 630 nm after the clearing protocols for human brain samples ($n = 6$). (G) Autofluorescence intensity of human brain samples after the clearing protocols ($n = 6$). Mean are shown. Scale bars indicate 4 mm. $**p < 0.01$ and $***p < 0.001$, see also **STAR Methods** for details.

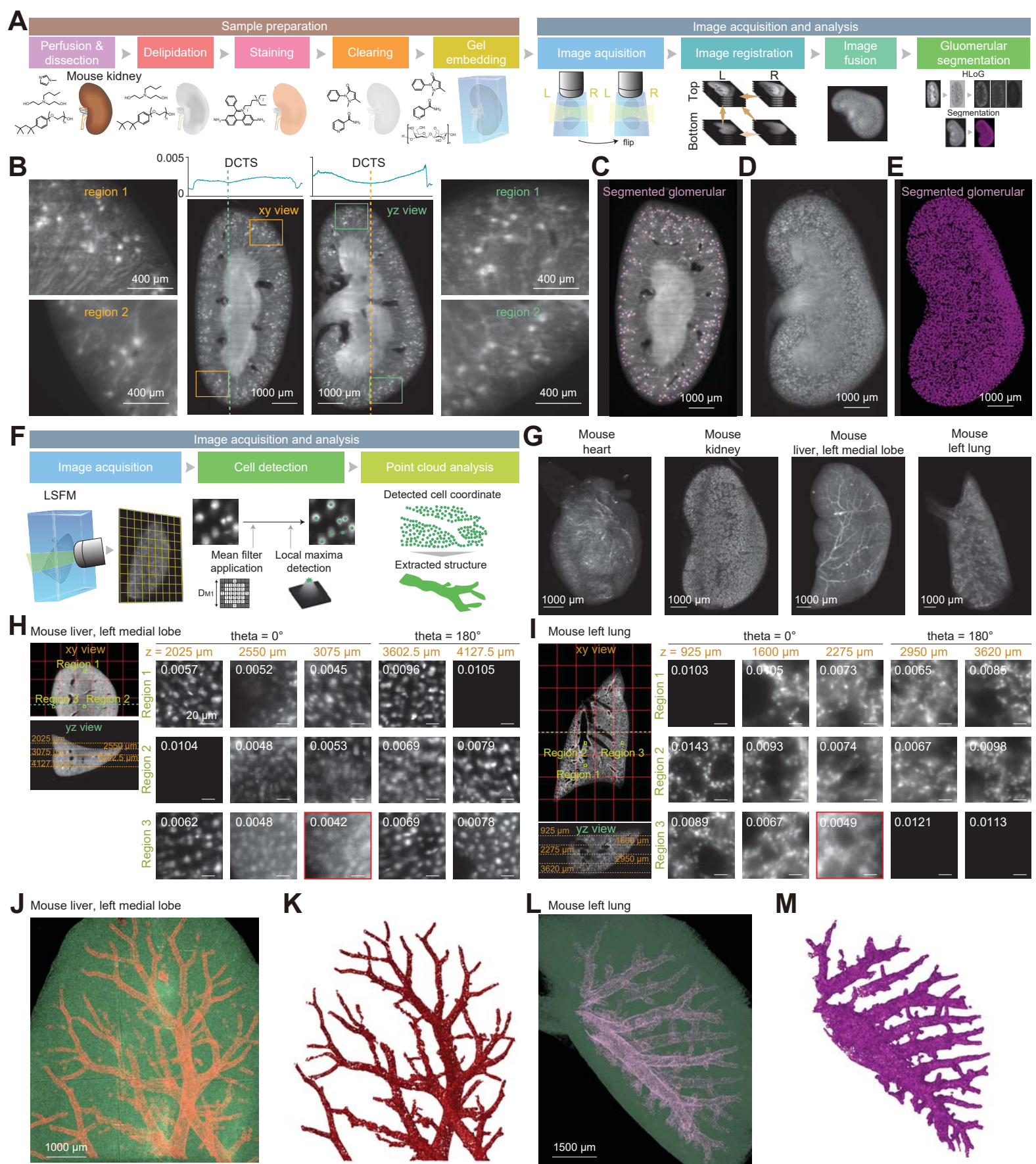


Figure S5

Figure S5. Comprehensive Cell Detection in Highly Cleared Mouse Organs by High-Resolution Imaging, Related to Figure 5.

(A) Scheme of CUBIC-based protocol for kidney glomerular segmentation. Samples were prepared using CUBIC protocol I. (B) Sectional images of multi-directionally fused images of kidney. The discrete cosine transformation Shannon entropy (DCTS) (Royer et al., 2016) is shown above the sectional images as an indicator of image quality. (C) Sectional image of segmented glomeruli of the kidney. Segmented renal glomeruli are shown in magenta. The renal glomeruli in the kidney were comprehensively analyzed by a Hessian-based difference of Gaussian (Zhang et al., 2015), see also **STAR Methods** for details. (D,E) Three-dimensional reconstitution of fused images of kidney (D), and segmented renal glomeruli (E). (F) Scheme of the CUBIC-based protocol for whole-organ cell analysis. (G) Volume-rendered mouse organ images obtained with high-resolution light sheet microscopy. Organs were stained with nuclear-staining dye. (H,I) Representative images of nuclear-stained liver (H) and lung (I). Images with the lowest DCTS are framed in red. DCTS value is shown in the upper-left corner of each image. (J,K) Partial liver is represented as an ensemble of detected cellular nuclei (“point cloud”). Tubular structures were extracted from the point clouds. (L,M) Point cloud representation of the left lung. Tracheas were extracted from the point clouds.

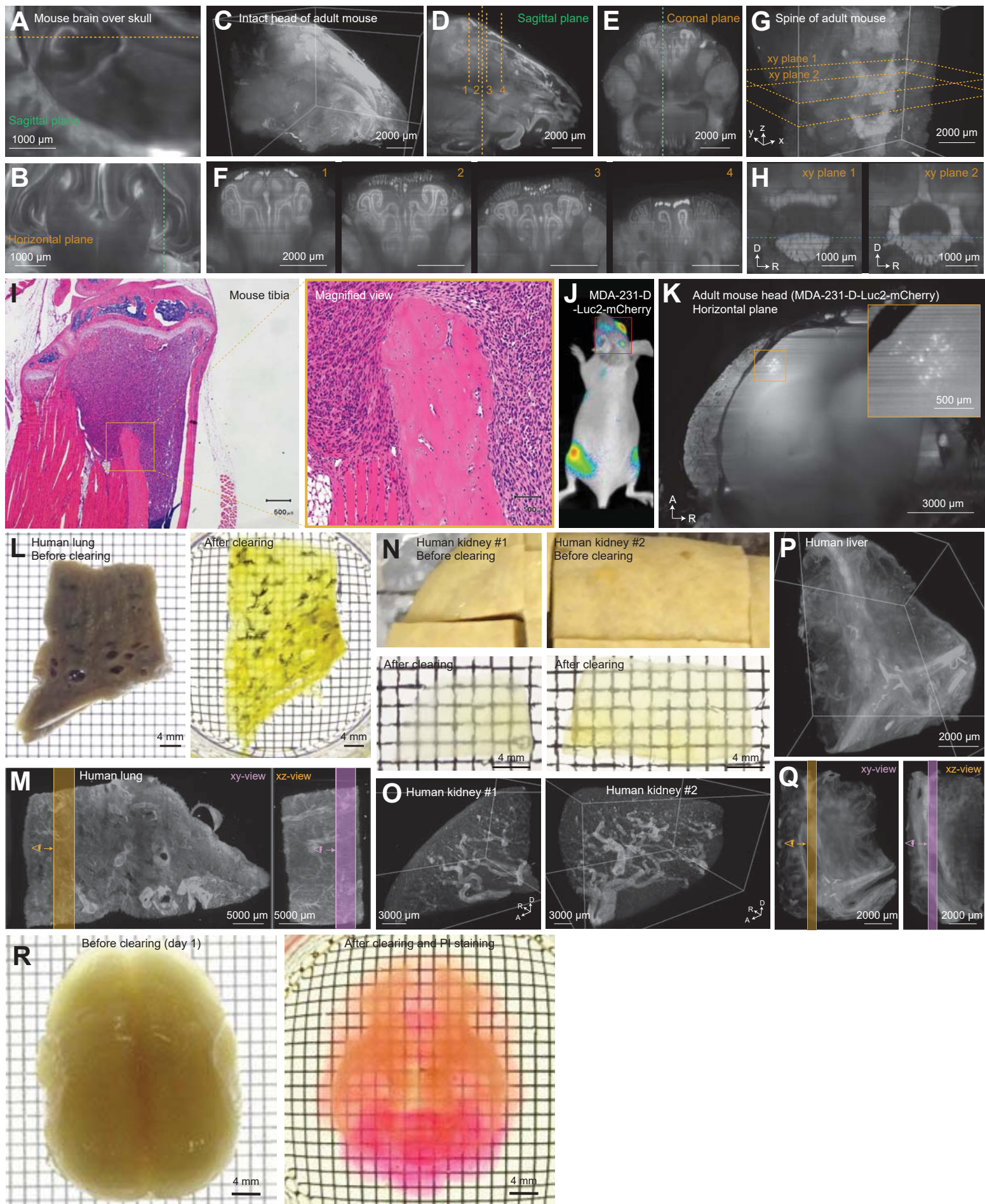


Figure S6

Figure S6. Scalable Imaging of Mouse and Primate Tissue, Related to Figure 6.

(A,B) Brain images of P7 mouse inside the skull. Sagittal plane (A) and horizontal plane (B) are shown. (C) Nuclear stained adult (8-week-old) mouse head. The head was cleared with CUBIC protocol II, and observed with LSM. (D,E) Sagittal and coronal section images of adult mouse head. Clear nasal structures were observed. (F) Serial sectional views of the nasal cavity. (G) Volume-rendered image of the spine (L4-L6) of an adult (8-week-old) mouse. Autofluorescence was observed. (H) Sectional images of the spine shown in G. (I) HE staining of the metastasized mouse tibia shown in Figures 6F-H. Infiltrating cancer cells can be clearly observed. (J) Bioluminescence imaging of a second individual MDA-231-D-injected immunodeficient BALB/c-nu/nu mouse. (K) Metastasized brain of the model mouse in J. Metastatic foci were clearly detected through the skull after the CUBIC II protocol. (L) Human lung before and after the clearing used in Figure 6I. (M) Human lung xy and xz views; maximal projection over a 3300- μ m-thick volume. The identical volumetric image shown in Figure 6I was re-analyzed. (N) Human kidney sample before and after clearing. (O) Volume-rendered image of the autofluorescence in dissected human kidneys. (P) Volume-rendered image of human liver tissue. (Q) Human liver xy and xz views; maximal projection over an approximately 650- μ m-thick volume. For L-Q, CUBIC protocol III was applied. (R) Adult marmoset brain was cleared by a modified CUBIC protocol I. The detailed experimental procedure is provided in the STAR Methods. Bright field images of the adult marmoset brain just after starting clearing (Day 1) and after complete clearing and staining are shown.

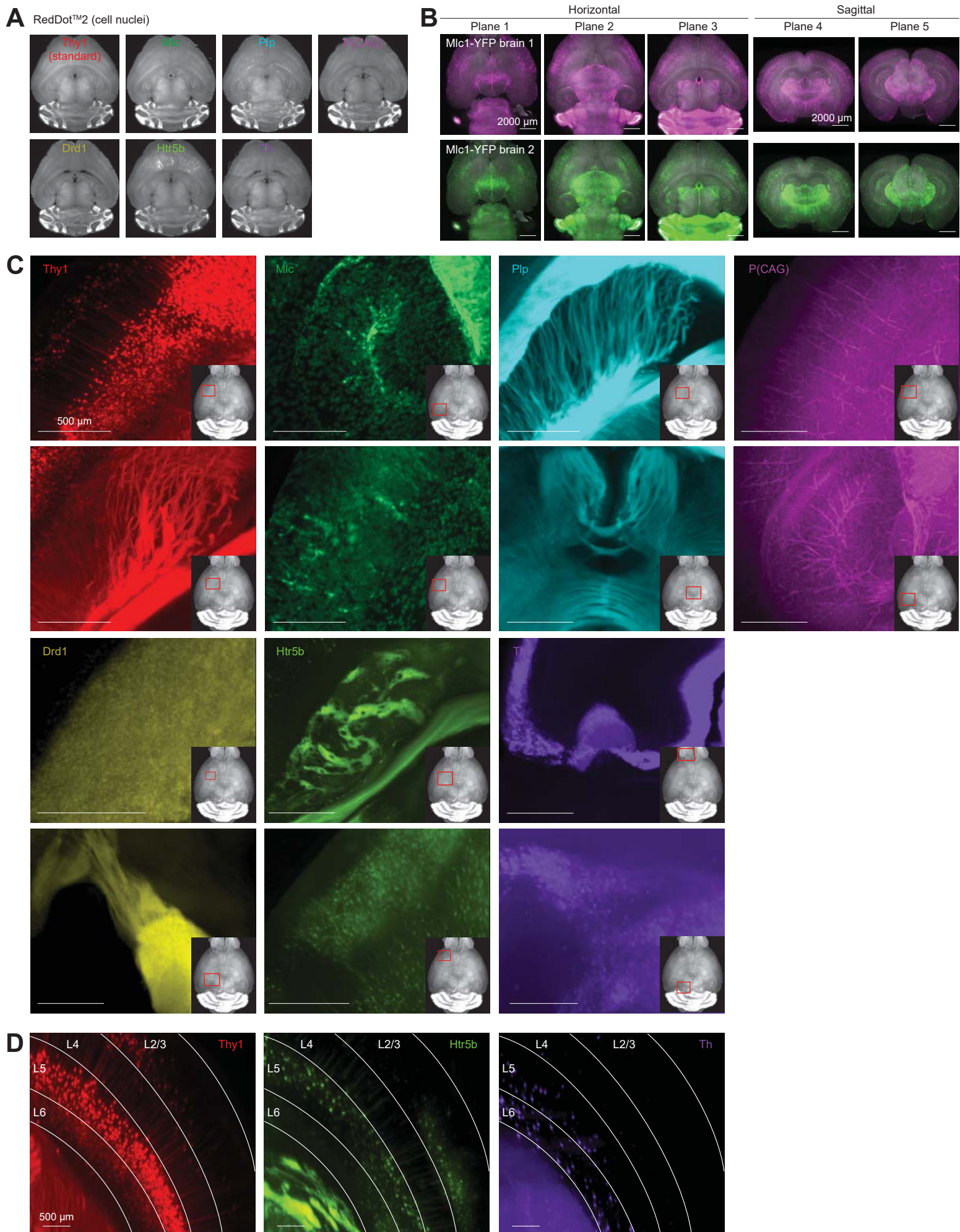
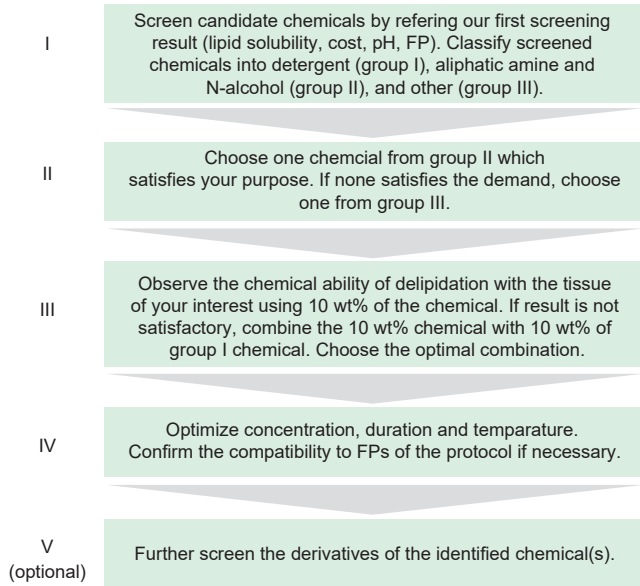


Figure S7

Figure S7. Virtual Multiplex Images of FP-expressing Brains Registered to a Standard Brain, Related to Figure 7.

(A) Volumetric images after non-linear registration. All of the nuclear stained images of genetic reporter mouse brains are displayed. Horizontal planes are shown. (B) To further verify the registration accuracy, two independent brains of the Mlc1-YFP reporter mouse were registered on the standard brain. After registration of the nuclear image, transformed YFP signals were observed. The YFP signals (magenta for brain 1, green for brain 2) were merged with the standard nuclear image (grey). Three horizontal section images and two coronal section images are shown. The YFP signal pattern was similar in the two brains, indicating that the registration was accurate. (C) Typical volume-rendered images of the seven types of FP-expressing brain. For navigation, each position of the acquired image is indicated in the inset image using the identical volumetric image of a nuclear-stained standard brain. (D) Individual expression pattern of the three different FPs shown in **Figure 7D**. The cortical layer structures are indicated.

A Procedures to develop customized delipidating chemical cocktails



B Procedures to develop customized RI matching chemical cocktails

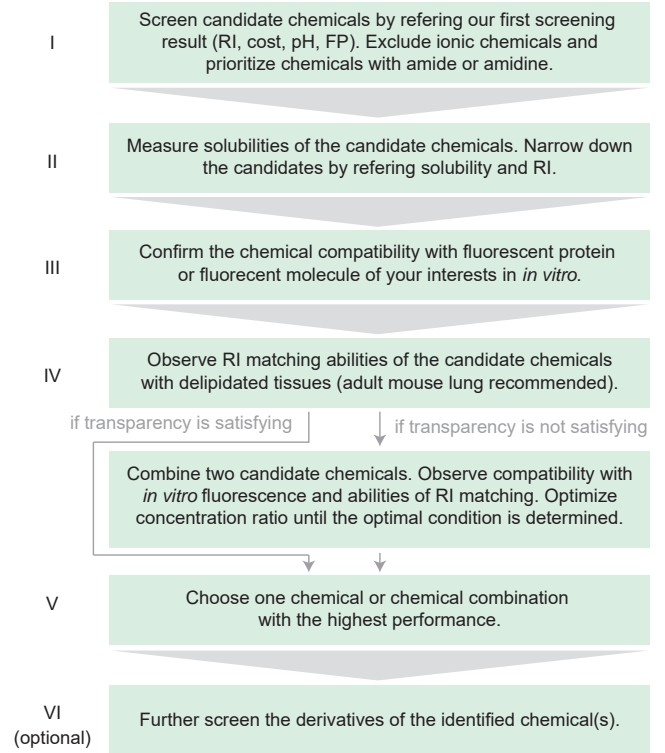


Figure S8

Figure S8. Flowcharts for Developing Customized Tissue-clearing Cocktails, Related to Figure 1.

(A) Procedure for developing customized delipidating chemical cocktails. **(B)** Procedure for developing customized RI-matching chemical cocktails.